



OPEN ACCESS

EDITED BY

Chaojin Lu,
University of Miami, United States

REVIEWED BY

Yanyang Zhao,
Shandong University of Science and
Technology, China
Guangwei Wang,
China University of Petroleum (East China),
China
Biao Chang,
China University of Geosciences Wuhan,
China

*CORRESPONDENCE

Chenggong Zhang
✉ batistutaqq@163.com

RECEIVED 28 February 2025

ACCEPTED 10 April 2025

PUBLISHED 09 May 2025

CITATION

Fu S, Zhang C, Liu H, Wei L, Bao H, Ye X,
Su Z, Chen H and Lin L (2025) Dolomites in a
carbonate-evaporite system: the fifth
member of the Middle Ordovician Majiagou
Formation, Eastern Ordos Basin, China.
Front. Mar. Sci. 12:1585055.
doi: 10.3389/fmars.2025.1585055

COPYRIGHT

© 2025 Fu, Zhang, Liu, Wei, Bao, Ye, Su, Chen
and Lin. This is an open-access article
distributed under the terms of the [Creative
Commons Attribution License \(CC BY\)](https://creativecommons.org/licenses/by/4.0/). The
use, distribution or reproduction in other
forums is permitted, provided the original
author(s) and the copyright owner(s) are
credited and that the original publication in
this journal is cited, in accordance with
accepted academic practice. No use,
distribution or reproduction is permitted
which does not comply with these terms.

Dolomites in a carbonate-evaporite system: the fifth member of the Middle Ordovician Majiagou Formation, Eastern Ordos Basin, China

Siyi Fu^{1,2,3,4}, Chenggong Zhang^{1,2,3*}, Hao Liu^{1,2,3}, Liubin Wei⁵,
Hongping Bao⁵, Xingchao Ye², Zhongtang Su^{1,2,3},
Hongde Chen^{1,2,3} and Liangbiao Lin^{1,2,3}

¹State Key Laboratory of Oil and Gas Reservoir Geology and Exploitation (Chengdu University of Technology), Chengdu, China, ²Institute of Sedimentary Geology, Chengdu University of Technology, Chengdu, China, ³Key Laboratory of Deep-time Geography and Environment Reconstruction and Applications of Ministry of Natural Resource, Chengdu University of Technology, Chengdu, China, ⁴College of Petroleum Engineering, China University of Petroleum, Beijing, China, ⁵Exploration and Development Research Institute of PetroChina Changqing Oilfield Company, Xi'an, China

Introduction: The carbonate-evaporite system contains substantial hydrocarbon resources and serves as an excellent subject for studying dolomitization problem. In the Ordos Basin, the fifth member of the Ordovician Majiagou Formation have extensive carbonate-evaporite deposits.

Methods: This study utilizes extensive drilling data, thin section microscopic examination, scanning electron microscopy, and a variety of geochemical analyses to investigate the origins of evaporites and the genesis of dolomites within this formation.

Results: Our findings indicate that the fifth member of the Majiagou Formation primarily contains two types of evaporites (halite and anhydrite) and five types of dolomites: micritic (Dol-1), fine-crystalline fabric-oblitative dolomite (Dol-2), fabric-retentive dolomite (Dol-3), microbial mats-associated dolomite (Dol-4), and medium-coarse crystalline dolomite (Dol-5). The evaporites, originating from seawater (sulfur isotope compositions ranging from 23.0 to 27.9 ‰), exhibit a planar distribution controlled by paleotopography and evaporation intensity, with distinct deposition centers for gypsum and halite. The eastern part of the study area is dominated by halite deposits, while both gypsum and halite are developed in the central region, and the western part is primarily characterized by gypsum deposition. LA-ICP-MS data indicate varying concentrations of MgCO₃ (34.4–44.3 wt%) and CaCO₃ (45.4–58.9 wt%), as well as trace elements including Na, Al, Si, K, Cu, Ba, Mn, and Fe. REE patterns and $\delta\text{Ce}/\delta\text{Eu}$ anomalies provide insights into dolomitization mechanisms.

Discussion: The formation of dolomites occurred in distinct stages. The first stage, from the penecontemporaneous to shallow burial periods, the formation of Dol-1, Dol-2, and Dol-3 through seepage-reflux dolomitization and evaporative pumping. Dol-4 also formed during this stage, closely associated with microbial dolomitization and influenced by tidal transport. The second

stage, during deep burial, resulted in Dol-5, which can be further categorized into Dol-5-1, formed by continued dolomitization from pore fluids, and Dol-5-2, formed through hydrothermal processes. The intensity of dolomitization is closely linked to the distribution of evaporites. Carbonates underlying gypsum strata exhibit a higher degree of dolomitization compared to those beneath halite strata. This is due to gypsum absorbing Ca^{2+} and releasing high-salinity brine during its transformation to anhydrite, thereby increasing the $\text{Mg}^{2+}/\text{Ca}^{2+}$ ratio in formation fluids. Consequently, the hydrocarbon resource potential of carbonate strata beneath gypsum layers is likely higher than that of those beneath halite layers.

KEYWORDS

Ordos Basin, carbonate-evaporite system, dolomitization, Majiagou Formation, Ordovician

Introduction

Carbonate–evaporite sequences are usually of interest to the oil industry because giant hydrocarbon accumulations have previously been discovered in dolomite reservoirs that are associated with evaporites (Kirkland and Evans, 1981; Wani and Al-Kabli, 2005; Warren, 2006; Jin et al., 2010; Peyravi et al., 2015; Shen et al., 2016; Jafarian et al., 2017; Kakemem et al., 2021). Therefore, the mechanism and timing of dolomite formation in carbonate–evaporite systems are aspects of commercial significance (Lu and Meyers, 1998; Lonnee and Machel, 2006; Ryan et al., 2020). The platform-scale dolomitization of limestone has been intensively studied, and several mechanisms, including evaporative pumping (Hsü and Siegenthaler, 1969; Iannace et al., 2011; Haas et al., 2015; Fu et al., 2019), seepage–reflux (Adams and Rhodes, 1960; Kaufman, 1994; Xiong et al., 2018), burial fluids (Qing and Mountjoy, 1994; Warren, 2000; Yang et al., 2018), hydrothermal (Middleton et al., 1993; Machel and Lonnee, 2002; Zhu et al., 2015; Dong et al., 2020), and microbial dolomitization (Vasconcelos et al., 1995; Lith et al., 2010), have been proposed. However, in carbonate–evaporite successions, the distribution of dolomite is not contiguous, and thus, existing models cannot adequately explain dolomitization. Recent studies have specifically investigated dolomitization processes for the deposition of dolostone in the evaporite settings, such as the change of salinity fluctuations (Kim et al., 2023), the microbial induced (Liu et al., 2019; Chang et al., 2020), and also hydrothermal dolomitization.

The Ordos Basin, which covers an area of approximately 250,000 km², contains the largest oil and gas field in China (Yang et al., 2008). The Ordovician Majiagou Formation in this basin has remained an active exploration target since the discovery of hydrocarbons in the formation in the early 1980s. According to previous studies, major carbonate–evaporite successions developed in the Majiagou Formation (Xiao et al., 2021), where evaporite

layers attained a maximum thickness of 150 m, and these extend laterally over an area of approximately 50,000 km². Although a series of study have been conducted on the evaporite-associated dolomites formation in the Majiagou Formation (Fu et al., 2019; Ding et al., 2021), but they still regard it as the thick layer dolomite, without considering the influence of evaporite on the dolomitization process. Therefore, this formation provides an opportunity to understand dolomitization associated with evaporites. In the present study, the mineralogy of the carbonate–evaporite succession was described and interpreted based on big data obtained from wells and outcrops that were partly provided by the Changqing PetroChina Oilfield Company. In addition, S isotopes, LA-ICP-MS *in-situ* trace and rare earth elements, and fluid inclusion homogenization temperature data will help us try to solve the problem of the nature and origin of dolomitization in the carbonate–evaporite depositional system.

Geological setting

The Ordos Basin is an intracratonic basin in Northern China, and it covers an area of approximately 25 × 10⁴ km² (Figure 1a). During the Ordovician, owing to subduction of the Qinling–Qilian paleo-ocean crust, the Ordos Basin developed between uplifts in the center–west of the area. Consequently, the East Ordos Basin evolved into a restricted open platform, which involved an intracratonic epeiric sea, with successive development of paleo-uplifts, restricted platforms, and evaporitic lagoon from west to east (Figure 1a), and sediments dominantly comprised interbedded shallow carbonates and evaporites (Chen et al., 2014) (Figure 1b). The Ordovician Majiagou Formation has been partitioned into six members (Ma 1–Ma 6) (Yang and Bao, 2011; Xiao et al., 2021), from the bottom to the top, and the fifth member (Ma 5) hosts the thickest evaporite layer. The Ma 5 has been divided into ten sub-members (Ma 5₁–Ma 5₁₀) (Figure 1c). The Ma 5₁–Ma 5₄, which exhibit evidence of

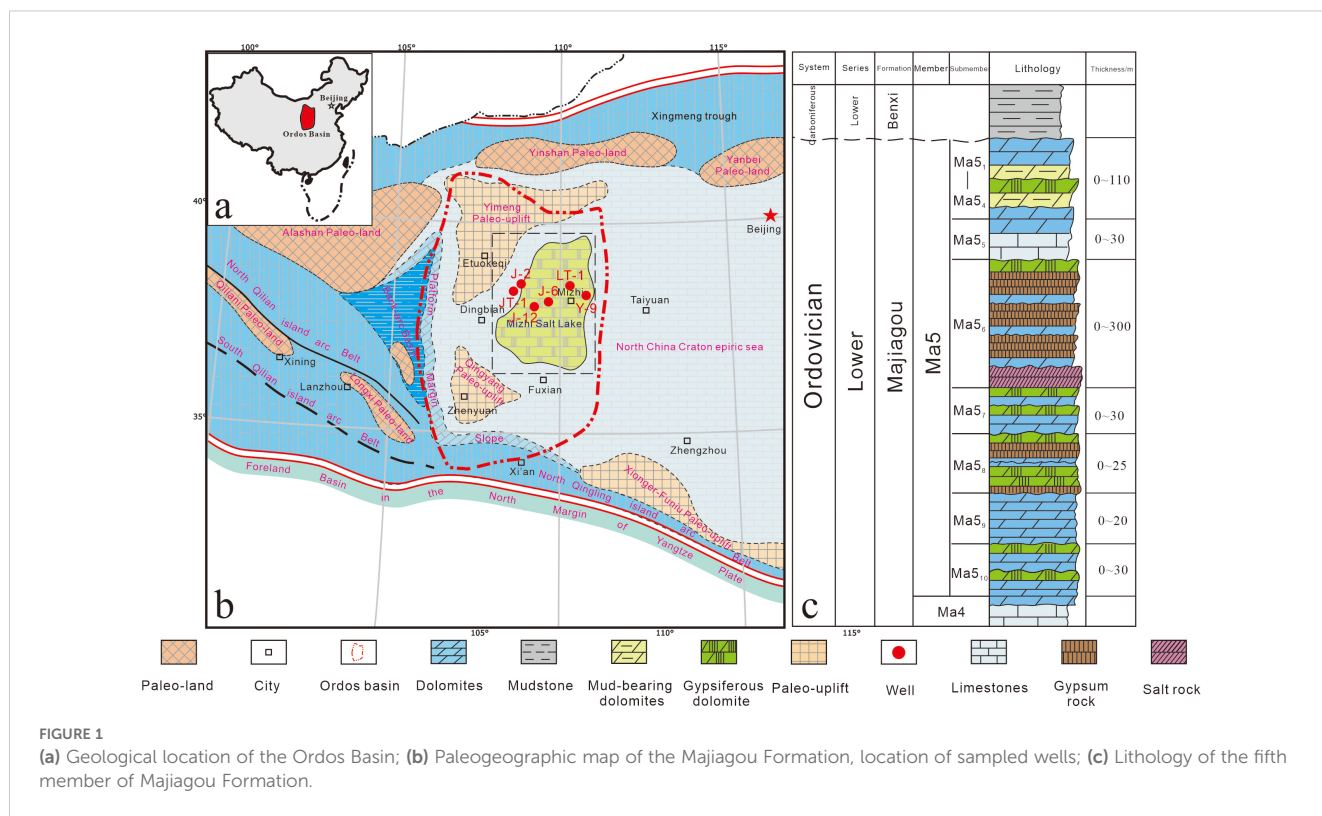


FIGURE 1

(a) Geological location of the Ordos Basin; (b) Paleogeographic map of the Majiagou Formation, location of sampled wells; (c) Lithology of the fifth member of Majiagou Formation.

karstification, comprise mainly muddy dolomite. The Ma₅ contains mostly limestone, fine-crystalline dolomite and microbial dolomite. The Ma₅₆–Ma₅₁₀ principally involve evaporites and carbonate, and the Ma₅₆, Ma₅₈, and Ma₅₁₀ contain multiple evaporites sedimentation, whereas the Ma₅₇ and Ma₅₉ involve mainly dolomites and few limestone (Xiong et al., 2019) (Figure 1c). Evaporites in the Ma₅₆ are the most widely distributed in the East Ordos Basin, and these vary in thickness from 20 to 300 m. Thus, the Ma₅₆ is often considered the boundary between sub- and pre-salt strata in the basin (Fu et al., 2019; Xiao et al., 2021), and the Ma₅₇ to Ma₅₉ (pre-salt strata), constitute the focus of the present study.

The thermal and tectonic history of the Ordos Basin has been intensively investigated (Zhao et al., 1996; Ren et al., 2014). Caledonian tectonic movements between the Late Ordovician and Middle Carboniferous uplifted and exposed sediments of the Majiagou Formation in the Ordos Basin. Consequently, numerous karst structures have formed on the Ma₅, and these host the Jingbian gas field (Li et al., 2008). Nevertheless, Ma₅₆ to Ma₅₁₀ were minimally impacted by karstification because of their distances from the weathering crust and the barrier effect of evaporites on the carbonates. In the Late Permian, sediments in the Ordos Basin were then buried to depths of approximately 3000 m, and sediments in the Majiagou Formation subsided further to depths exceeding 4500 m in the Middle Cretaceous. Starting from approximately 60 Ma, uplift and erosion of approximately 1000 m occurred in response to activities in the Qinghai–Tibet Plateau that were caused by the collision of the Indian and Eurasian plates during the Himalayan Orogeny (Zhao et al., 1996).

Samples and analytical methods

The 148 samples analyzed in the present study were collected from 26 wells, and six of these (wells JT-1, J-2, J-6, J-12, LT-1, and Y-9) penetrated the entire succession of the Majiagou Formation are the key wells (Figure 1b). In the east of the study area, the thick halite in wells LT-1 and Y9 revealed its continuous deposition in the Ma₅₆. Conversely, in the center of the study area, wells J-6 and J-12 showed that the Ma₅₆ contains mainly anhydrite and gypsiferous dolomite. In the west, wells J-2 and JT-1 demonstrated that the Ma₅₆ is dominated by dolomite, whereas anhydrite is rare. The sequential collection of samples from different locations can facilitate understanding of the correlation between evaporites and dolomite. Petrographic studies using 148 thin sections that were stained with Alizarin Red S in the State Key Laboratory for Oil and Reservoir Geology and Exploration, Chengdu University of Technology, enabled detailed characterization of dolomite types.

Based on the examination of cores, 16 dolomite samples were selected for field emission scanning electron microscopy (FE-SEM) in the State Key Laboratory for Oil and Gas Reservoir Geology and Exploitation, Chengdu University of Technology. FE-SEM investigations were performed using a Quanta 250 FEG equipped with an Oxford INCAx-max20 system. The best resolution in the high-vacuum mode was approximately 1.2 nm and the magnification ranged from 50 to 10⁶.

Homogenization temperature experiments were conducted in the same laboratory on 26 samples using the THMSG-600 heating-cooling stage that was designed and manufactured by Linkam (UK). Prior to inclusion temperature measurements, standards were

utilized to test the heating and cooling system, as well as to calibrate the instrument. Homogeneous temperatures (a precision of 0.1°C) were obtained via cyclic testing using a heating rate of 5°C/min, and the temperature in the laboratory was 23.5°C.

Sulfur isotope analyses of halite, anhydrite, and gypsiferous dolomite were conducted in the Institute of Geology and Geophysics, Chinese Academy of Sciences, using a MAT 251 mass spectrometer. Details on the sulfur extraction from carbonate samples for isotope analysis are available in [Wotte et al. \(2012\)](#). The precision for the $\delta^{34}\text{S}$ analysis was better than 0.3‰, and the Canyon Diablo troilite (CDS) was utilized as the standard ([Cai et al., 2001](#)).

Major and trace element analyses were conducted using an LA-ICP-MS in the State Key Laboratory of Ore Deposit Geochemistry, Institute of Geochemistry, Chinese Academy of Sciences. Measurements were performed using an Agilent 7500x ICP-MS that is equipped with a GeoLas Pro 193 nm ArF excimer laser. Elemental concentrations were calibrated against multiple reference materials (GOR128-G, ATHO-G, StHs6/80-G, and T1-G) and internal standards ([Chen et al., 2011](#)). Data correction and calibration were performed using the ICPMSDataCal ([Liu et al., 2008a; Liu et al., 2008b](#)). Surfaces of samples were ablated using laser pulses (4 Hz) for approximately 40 s after monitoring of the gas blank for 20 s, and the associated signals were used to select intervals that excluded inclusions and zoning ([Zhao and Zhou, 2015](#)). The normalization for rare earth elements is exemplified by europium (Eu), where the measured concentration is normalized against the North American Shale Composite (NASC) reference value to obtain Eu_N . The anomaly parameter δEu is subsequently derived through the relationship: $\delta\text{Eu} = 2\text{Eu}_N/(\text{Sm}_N + \text{Gd}_N)$, incorporating adjacent element ratios to mitigate chondritic normalization artifacts.

Results

Mineralogy and petrography

Petrographic observations showed that the dominant evaporite minerals in samples that were analyzed are halite and anhydrite. Dolomites in the study area can be divided into the following types: micritic (Dol-1), fine-crystalline fabric-obliterative dolomite (Dol-2), fabric-retentive dolomite (Dol-3), microbial mats-associated dolomite (Dol-4), and medium-coarse crystalline dolomite (Dol-5). Among the carbonate-evaporite sequences in the study area, Dol-1 and Dol-2 are the most common.

Halites

Petrographic analysis reveals two types of halite development in the Ma 5 sub-members of the Ordos Basin that exhibit similar mineral assemblages. The type 1 halite comprises light gray pore-filling materials, which are characterized by irregular shapes and sizes of 0.1–15 mm ([Figure 2a](#)). This halite type is common in the uppermost parts of the Ma 5₇ and Ma 5₉. The type 2 halite exhibits

textures that vary from massive to bedded ([Figure 2b](#)), and this is frequent in the Ma 5₆ and Ma 5₈. The type 2 halite displays varying colors, including gray, white, and red ([Figure 2c](#)). In vertical succession, the gray halite is usually at the base, followed by the white and red varieties ([Figure 2d](#)).

Anhydrites

The anhydrite types that were identified in samples analyzed can be grouped into the following: bedded ([Figure 3a](#)), nodular ([Figure 3b](#)), and vug-filling ([Figure 3c](#)).

Bedded anhydrites mainly occur in the Ma 5₆ and Ma 5₈, and these range in thickness from < 10 cm to several meters. The cumulative thickness of bedded anhydrites in well J-4 exceeds 80 cm in the middle of study area. Microcracks filled with argillaceous materials and deformation structures in these bedded anhydrites are attributed to the fluid characteristics of evaporites ([Warren, 2006](#)). Under a microscope, bedded anhydrites commonly occur as prismatic, cuboidal, or parallel veins of crystals ([Figure 3d](#)).

Nodular anhydrites are common between the mudstone and dolomite layers in M5₆ and M5₈. These nodules vary in size from a few mm to 5 cm, and their shapes vary from oval to irregular. Locally, these nodules represent up to 80% of the volumetric fraction of samples, and dolomites occur as thin laminae on their surfaces, thereby producing a chicken-wire structure.

Vug-filling anhydrites are found in dolomitic and fine-crystalline dolomite reservoirs. Vugs display irregular shapes, and the milky white anhydrites are typically 1–10 mm in length. Under a polarized light microscope, these anhydrites occur as blocky and prismatic crystals ([Figure 3e](#)).

Dolomites

The Dol-1 comprises crystals that are < 20 μm , and this occurs at times as discontinuous horizontal veins ([Figure 4a](#)). The Dol-1 is associated with argillite, pyrite, and gypsum ([Figures 4b, c](#)), which suggests that it is part of a tidal-flat facies that involved high evaporation. In this dolomite, primary pores are undeveloped, but occasional dissolution pores and fractures that are filled with anhydrite are present. The intrusion of anhydrite crystals into the Dol-1 indicates that the former was formed earlier ([Figure 4c](#)).

The Dol-2 is the most common type of dolomite in the study area, and because the size of its crystals ranges from 20–150 μm , its primary structure is difficult to observation under the microscope. This dolomite type is dominated by dark euhedral to subhedral crystals ([Figure 4d](#)), and these crystals are locally associated with stylolites.

The Dol-3, which is assigned a high-energy environment in tidal flat facies, primarily contains particles ranging in size from 200–500 μm , and these involve irregular crystals of 50–100 μm ([Figure 4e](#)). Interstices between these particles are filled with fine (10–30 μm) dolomite cement, whereas pores associated with intergranular dissolution are typically filled with organic matter and quartz ([Figure 4f](#)).

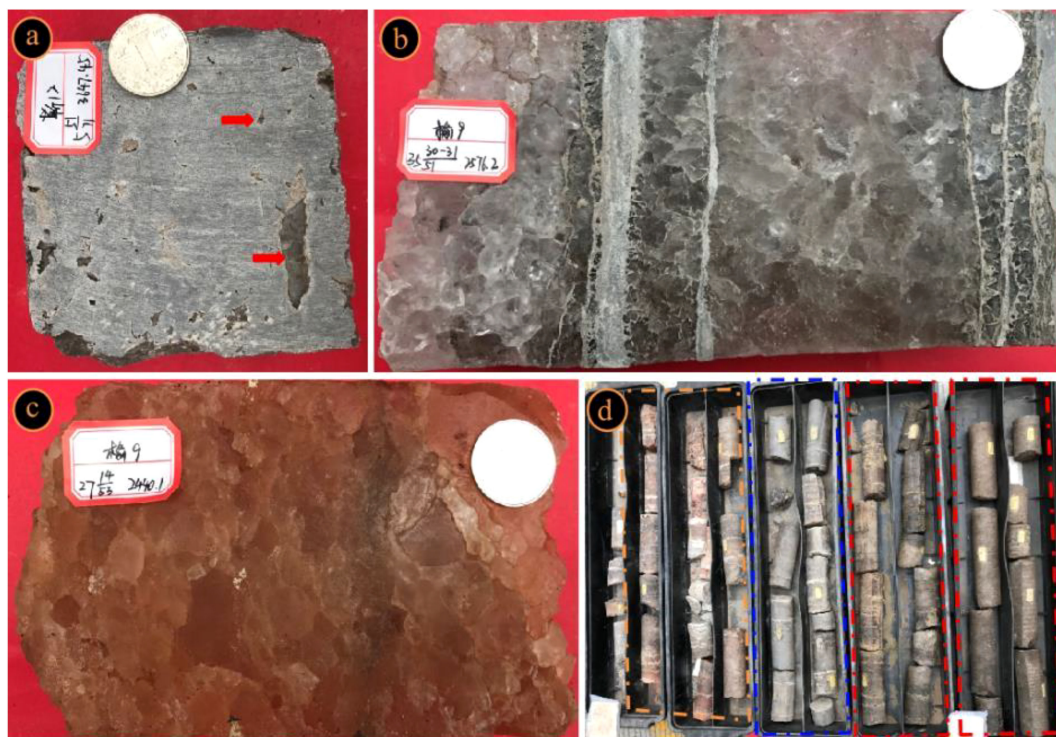


FIGURE 2

Well core images of halite features. **(a)** Well J12, 3647.95 m. Numerous dissolved pores have been filled by halite (red arrows). **(b)** Well Y9, 2576.2 m. Gray to white halite with thinly laminated anhydrite. **(c)** Well Y9, 2440.1 m. Close-up of the red halite. **(d)** Well F5, 2308.37 - 2317.00 m. Panoramic view of the part of the halite showing three distinct halite beds, gray halite (red box), white halite (blue box) and red halite (yellow box) from the lower to the upper parts.

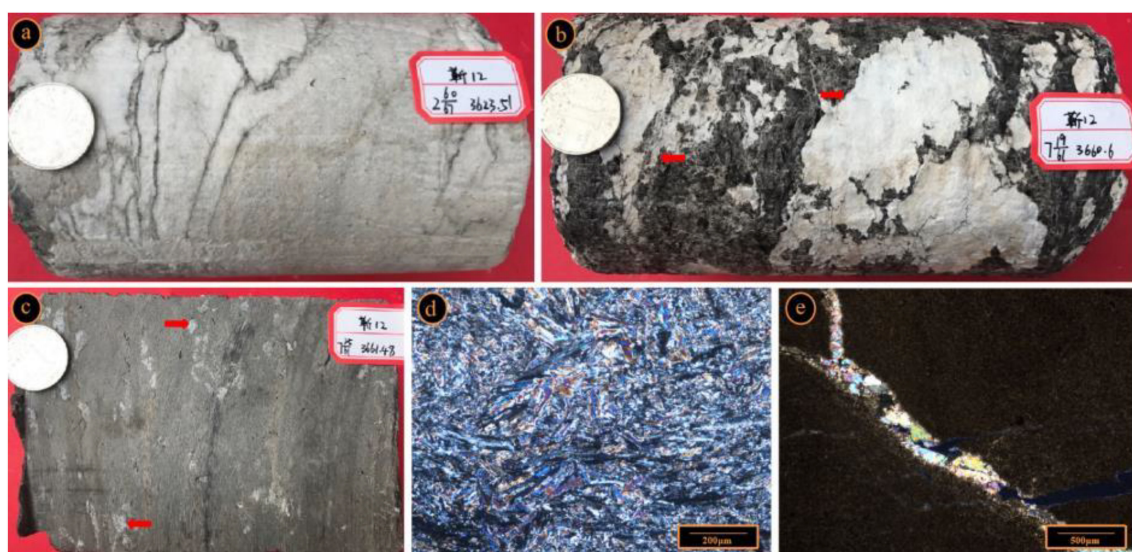


FIGURE 3

Well core images of anhydrite features. **(a)** Well J12, 3623.51 m. Bedded anhydrite with muddy stripes. **(b)** Well J12, 3660.60 m. Anhydrite nodules (red arrows). **(c)** Well J12, 3661.48 m. Numerous dissolved pores have been filled by anhydrite (red arrows). **(d)** Well J12, 3661.48 m. Details of anhydrite crystal. Cross polar. **(e)** Well J6, 3615.84 m. Detail of anhydrite filling micro-fractures. Cross polar.

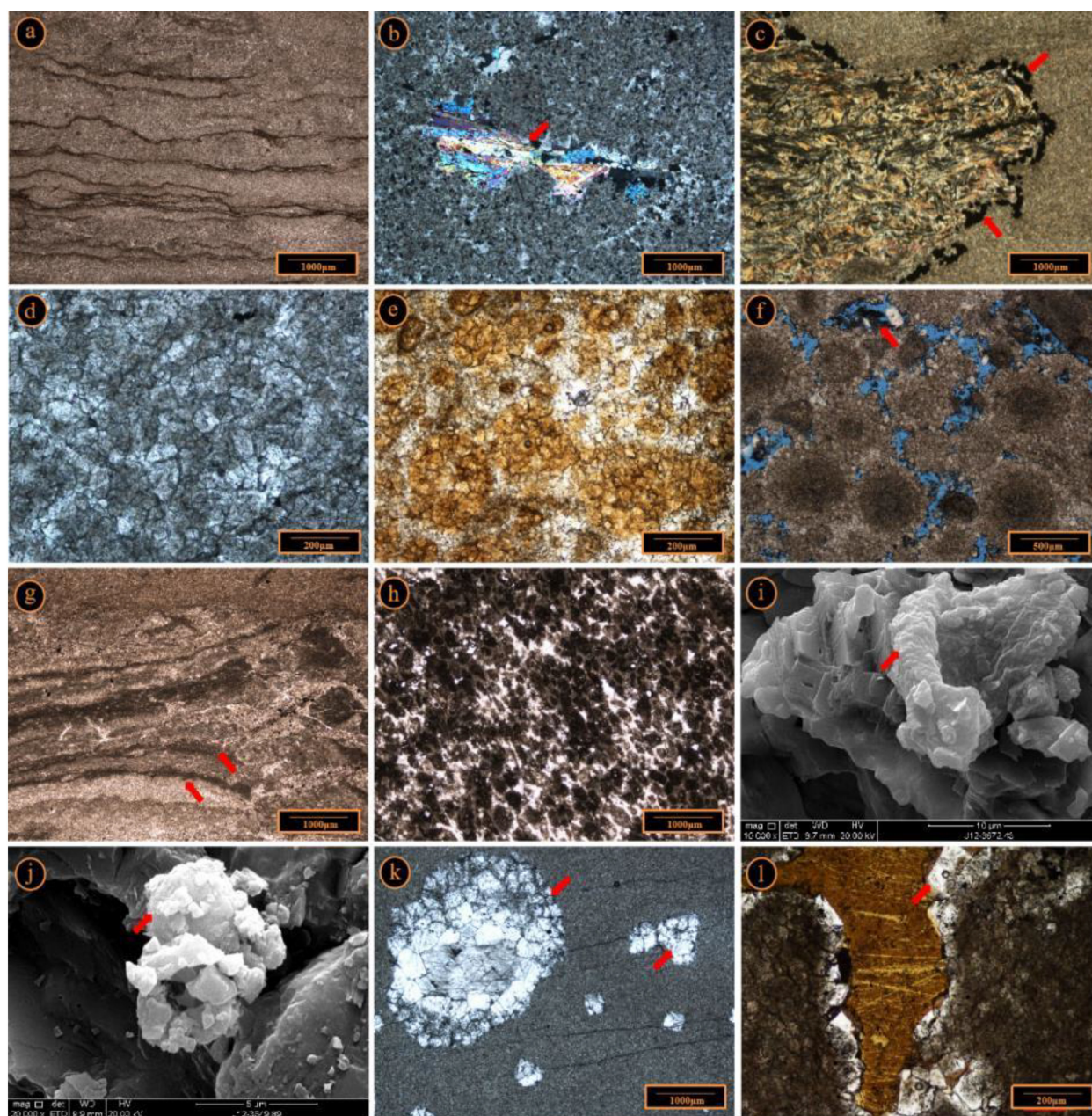


FIGURE 4

Microphotographs of different types of dolomites. (a) Well J6, 3573.37 m. Dol-1 with thin-layered mudstone. Transmitted light. (b) Well J6, 3562.17 m. Anhydrite (red arrow), Dol-1. Cross polar. (c) Well J12, 3620.11 m. Detail of anhydrite rushed into the dolomite, note the boundaries of pyrite (red arrows), Dol-1. Cross polar. (d) Well J6, 3670.50 m. Dol-2. Transmitted light. (e) Well J12, 3616.75m. Fabric-retentive dolomites composed of brown particles and white cements, Dol-3. Transmitted light. (f) Well T38, 3612.00 m. Oolitic dolomite, interparticle dissolution pore have been filled by organic matter (red arrow) and quartz, Dol-3. Transmitted light. (g) Well J12, 3649.80 m. Details of layered stromatolite dolomite, Dol-4. Transmitted light. (h) Well J6, 3585.07 m. Details of Thrombolite dolomite, Dol-4. Transmitted light. (i) Well J12, 3649.89 m. Close-up view of spherical extracellular polymeric substances, Dol-4. SEM. (j) Well J12, 3672.43 m. Close-up view of tubular extracellular polymeric substances, Dol-4. SEM. (k) Well JT1, 2529.1 m. Example of medium to coarse crystalline dolomite (red arrows), Dol-5. Transmitted light. (l) Well J12, 3620.11 m. Example of serrated dolomite cement (red arrows), Dol-5. Transmitted light.

The Dol-4 is commonly observed in M5₇ and M5₉ sub-members, and it is characterized by agglutinated, calcified, and spar-encrusted microbe macro-fabrics (Riding, 2000). It comprises stromatolitic and thrombolitic dolomites (Figures 4g, h). In the study area, thrombolites appear to be primary, whereas

stromatolites are secondary. SEM observations reveal that some of these dolomites were microbially precipitated. Spherical and tubular extracellular polymeric substances (EPS) on surfaces of crystals of this dolomite support its association with microbes (Figures 4i, j).

The Dol-5 can be further subdivided into two types: Type 1 (Dol-5-1) predominantly occurs as euhedral to subhedral crystals in paragenetic association with Dol-1 and Dol-2, showing crystals varying in size from 200–1000 μm (Figure 4k). These crystals are brighter than those of surrounding rocks, and some crystals exhibited a wavy extinction. Type 2 is serrated dolomite cement, which is characterized by grain sizes of 200–300 μm . It is mainly developed along the edges of intergranular solution pores in fine crystalline dolomites (Figure 4l). Crystals of this type of dolomite, which are commonly serrated and rectangular, are also generally brighter than those of surrounding fine crystalline dolomites.

Fluid inclusions

Considering that fluid inclusion data for the Dol-1, Dol-2, and Dol-3 have been reported in previous studies (Su et al., 2017), in the present study, analysis of fluid inclusions was conducted primarily using samples of the Dol-5, and results are presented in Table 1. Homogenization temperatures were determined using nine samples (Figure 5), and these yielded 29 points for the type 1 Dol-5 (Dol-5-1) and 18 for the type 2 (Dol-5-2). Therefore, 47 temperature measurements were obtained from these dominantly single-phase and liquid-filled inclusions. Shapes of the inclusions range from irregular to globular, and the longest diameters vary between 1 μm and 12 μm . The clustering of homogenization temperatures

indicate that initial characteristics of the inclusions were minimally altered (Jiang et al., 2014). Coarse dolomites associated with the dolomicrite (Dol-5-1) produced mean homogenization temperatures ranging from 110–130 $^{\circ}\text{C}$, whereas dolomite cements (Dol-5-2) display homogenization temperatures varying from 80–100 $^{\circ}\text{C}$ (Figure 6).

S isotope compositions

Evaporite samples that were analyzed produced $\delta^{34}\text{S}$ values ranging from 23.0–27.9 ‰ (Table 2), whereas anhydrites associated with dolomite values varying from 23.0–27.8 ‰. Data for bedded anhydrites and halites range from 24.5 to 28.8 ‰ and 26.4 to 27.0 ‰, respectively.

Major and trace elements

Some spots of analyses of major and trace elements in various types of dolomites using LA-ICP-MS are shown in Figures 7, 8. Elemental composition data for dolomites are partly shown in Tables 3, 4.

The MgCO_3 and CaCO_3 concentrations of different types of dolomite in the M5 member ranges from 34.4 to 44.3% and 45.4 to 58.9%, respectively. The Na, Al and Si concentration in dolomite

TABLE 1 Homogenization temperatures of Dol-5 analysis.

Types	Sample Number	Shape of Inclusions	Size of Inclusions (μm)	Temperature ($^{\circ}\text{C}$)	Salinity (wt%)
Dol-5-1	YT1-2529.10-1	oval	4	122	/
	YT1-2529.10-2	triangular	7	123	/
	YT1-2529.10-3	oval	6	102	/
	YT1-2529.10-4	rectangular	6	117	17.19
	YT1-2529.10-5	square	5	125	16.53
	YT1-2529.10-6	globular	5	127	17.55
	YT1-2529.10-7	rectangular	6	115	17.19
	YT1-2534.02-1	oval	5	129	9.47
	YT1-2534.02-2	oval	4	134	12.42
	YT1-2534.02-3	square	6	132	/
	YT1-2534.02-4	rectangular	5	130	/
	J12-3642.41-1	oval	8	135	/
	J12-3642.41-2	rectangular	12	114	12.53
	J12-3642.41-3	oval	7	125	11.11
	J12-3642.41-4	irregular	8	112	/
	J12-3642.41-5	rectangular	5	130	11.23
	J6-3599.37-1	oval	5	129	9.47
	J6-3599.37-2	oval	4	134	12.42

(Continued)

TABLE 1 Continued

Types	Sample Number	Shape of Inclusions	Size of Inclusions (μm)	Temperature ($^{\circ}\text{C}$)	Salinity (wt%)
	J6-3599.37-3	square	6	132	/
	J6-3599.37-4	rectangular	5	130	/
	J6-3599.37-5	oval	8	135	/
	J6-3599.37-6	rectangular	12	114	12.53
	J6-3599.37-7	oval	7	125	11.11
	J6-3599.37-8	irregular	8	112	/
	J6-3556.90-1	rectangular	5	130	11.23
	J6-3556.90-2	oval	6	113	/
	J6-3556.90-3	oval	5	115	11.83
	J6-3556.90-4	rectangular	7	112	11.71
	J6-3556.90-5	oval	10	115	10.74
Dol-5-2	J6-3581.30-1	rectangular	5	95	/
	J6-3581.30-2	oval	5	93	18.7
	J6-3581.30-3	square	4	92	18.09
	J6-3581.30-4	oval	3	92	17.74
	J6-3581.30-5	square	7	82	/
	J6-3581.30-6	rectangular	9	81	/
	J6-3581.30-7	rectangular	9	85	/
	J12-3639.80-1	oval	5	98	/
	J12-3639.80-2	rectangular	7	94	/
	J12-3639.80-3	oval	4	94	/
	J6-2556.30-1	irregular	8	101	/
	J6-2556.30-2	oval	7	95	/
	J6-2556.30-3	oval	5	92	/
	J6-2556.30-4	oval	10	95	/
	YT1-2532.07-1	irregular	8	96	/
	YT1-2532.07-2	globular	3	98	/
	YT1-2532.07-3	oval	6	104	/
	YT1-2532.07-4	oval	5	98	/

between 10.3 to 351.5 ppm, 4.4 to 903.3 ppm and 59.6 to 2717.6 ppm, respectively. The K, Cu and Ba concentration in dolomite between 0.8 to 1074.9 ppm, 0.1 to 3.7 ppm and 0.1 to 47.8 ppm, respectively. Mn and Fe concentration in dolomite ranges between 15.0 to 57.2 ppm and 111.6 to 3877.4 ppm, respectively.

The ΣREE values of Dol-1, Dol-2, Dol-3, Dol-5 dolomites range from 2.17 to 19.98 ppm, whereas the ΣREE values of Dol-4 range from 1396.71 to 1841.32. The REE date in this paper has been normalized to the North America Shale Composite (Haskin et al., 1968). The δCe and δEu of different dolomite range from 0.84 to 2.30 and 0.05 to 2.05, respectively.

Distribution of evaporites

Based on data from more than 200 wells, the Ma 5₆ was found to contain the most extensive and thickest evaporites in the study area. Thickness distribution maps of the bedded anhydrite and halite in the Ordos Basin for this sub-member are shown in Figure 9. The occurrence of evaporites spans a distance of approximately 340 km in the North–south direction and approximately 160 km in the East–west direction. Regarding halite, the thickest occurrence of approximately 150 m is near well Y9 in the Eastern Ordos Basin. It extends over lateral distances of approximately 260 km from the

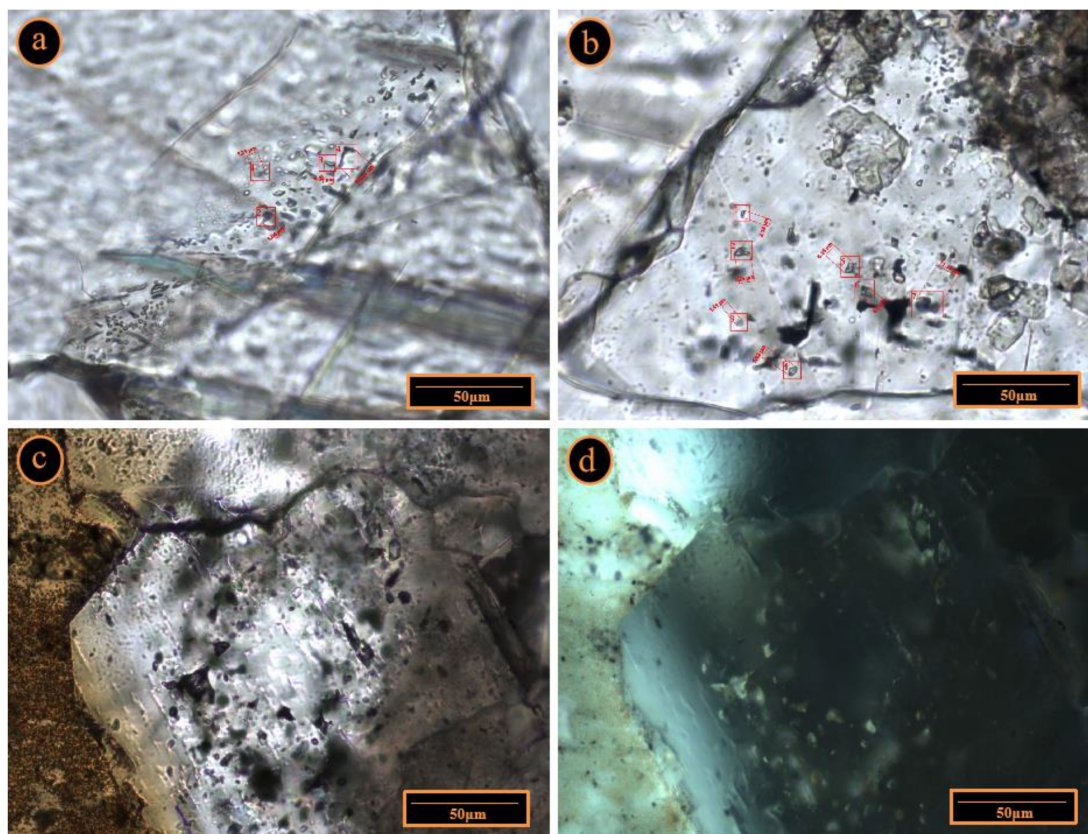


FIGURE 5
Photomicrographs of hydrocarbon inclusions under transmitted light and UV light. (a, b) Well YT1, 2529.1 m. Hydrocarbon inclusions in Dol-5-1 across cleavage crack. Transmitted light. (c) Well J6, 3581.30 m. Hydrocarbon inclusions in Dol-5-2. Transmitted light. (d) Well J6, 3581.30 m. Hydrocarbon inclusions in Dol-5-2 with blue fluorescence. UV light.

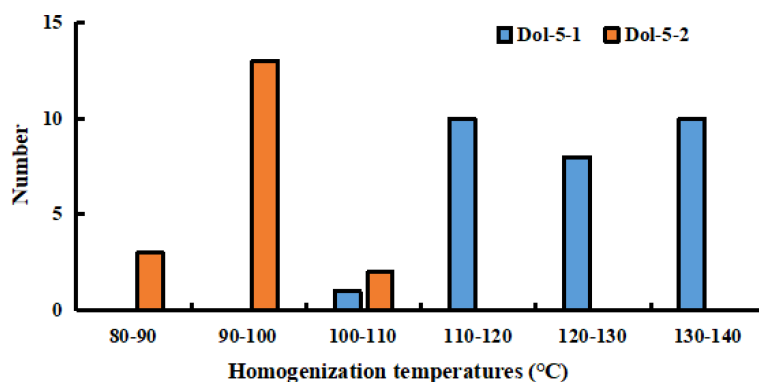


FIGURE 6
Homogenization temperatures measured from inclusions of Dol-5 from the Ordovician Majiagou Formation.

north to south and 100 km from the east to west. Conversely, the bedded anhydrite is thickest (40 m) near well JT1 in the Western Ordos Basin.

Stratigraphic correlation of the Majiagou Formation from the west to the east of the Ordos Basin (Figure 10) reveals similar

distribution characteristics for evaporites. Halite is widely distributed in the central portion of the eastern region, whereas anhydrite is mainly distributed in the west. Further, dolomite contents of carbonates decrease considerably from the west to east.

TABLE 2 $\delta^{34}\text{S}$ values of evaporites in the Ordovician Ma 5 Formation.

Sample Number	Members	Minerals	$\delta^{34}\text{S}(\text{‰})$
J12-2	Ma 5 ⁷	Gypseous dolomite	27.8
J6-2	Ma 5 ⁷	Gypseous dolomite	23.0
Y9-3	Ma 5 ⁶	Gypseous dolomite	24.4
Y9-4	Ma 5 ⁸	Gypseous dolomite	24.2
T17-1	Ma 5 ¹⁰	Gypseous dolomite	24.1
F5-1	Ma 5 ⁶	Halite	27.0
Y9-1	Ma 5 ⁶	Halite	26.4
J12-1	Ma 5 ⁶	Anhydrite	27.9
J6-1	Ma 5 ⁸	Anhydrite	28.8
Y9-2	Ma 5 ⁸	Anhydrite	24.5

Discussion

Salt minerals

The origin of evaporites has been usually explained using two models. In the first, during the active tectonic period, the associated high temperatures and squeezing induced upwelling of brines from depth, and rapid cooling of these brines caused precipitation of salts. Owing to its high density and strong fluidity, salts accumulated gradually in the depression, thereby forming evaporites in the center of the basin (Manzi et al., 2012; Zhou et al., 2011; Zhang et al., 2016). In the second, in many studies,

evaporites in sedimentary basins are assigned an origin from seawater (Treesh and Friedman, 1974; Ji et al., 2005). Arid and hot conditions promote the continuous evaporation of restricted seawater. If the addition of external seawater is considerably lower than the intensity of evaporation, the salinity of the restricted seawater continuously increases, and eventually precipitation occurs and different types of evaporites are deposited. The $\delta^{34}\text{S}$ data can adequately explain the source of evaporites (Jiang et al., 2014). Those $\delta^{34}\text{S}$ values of halite and anhydrite from the Majiagu Formation varying from 24.2‰ to 28.8‰, and these values are within the range of 26.0–34.0‰ that were reported for anhydrites derived from Ordovician seawater by Claypool et al. (1980). As mentioned earlier, hydrothermal mineral is not developed by our observation. These results suggest that sulfur in samples from the study area was derived from seawater rather than from brines in deep sections of the basin.

Minerals from the edge to the center of the lagoon generally comprise a transition from carbonates to anhydrite/gypsum, followed by halite, and this is caused by changes in the seawater salinity (Hovorka, 1992; Manaa and Aref, 2022). Warren (2006) noted that minerals present depend on the evaporation intensity. As seawater evaporation reaches 68%, precipitation of gypsum is initiated, whereas that of halite commences at an evaporation value of 88%. In addition, the deposition of evaporite minerals is affected by the accommodation space, evaporation rate, and seawater replenishment intensity (Hsü et al., 1978; Sun et al., 1995; Schreiber and Tabakh, 2000; Natalicchio et al., 2021; Mitchell et al., 2021). As shown in Figure 10, the depocenter of evaporites in the study area was around Mizhi, and the boundary between the anhydrite and halite deposition areas is near Jingbian.

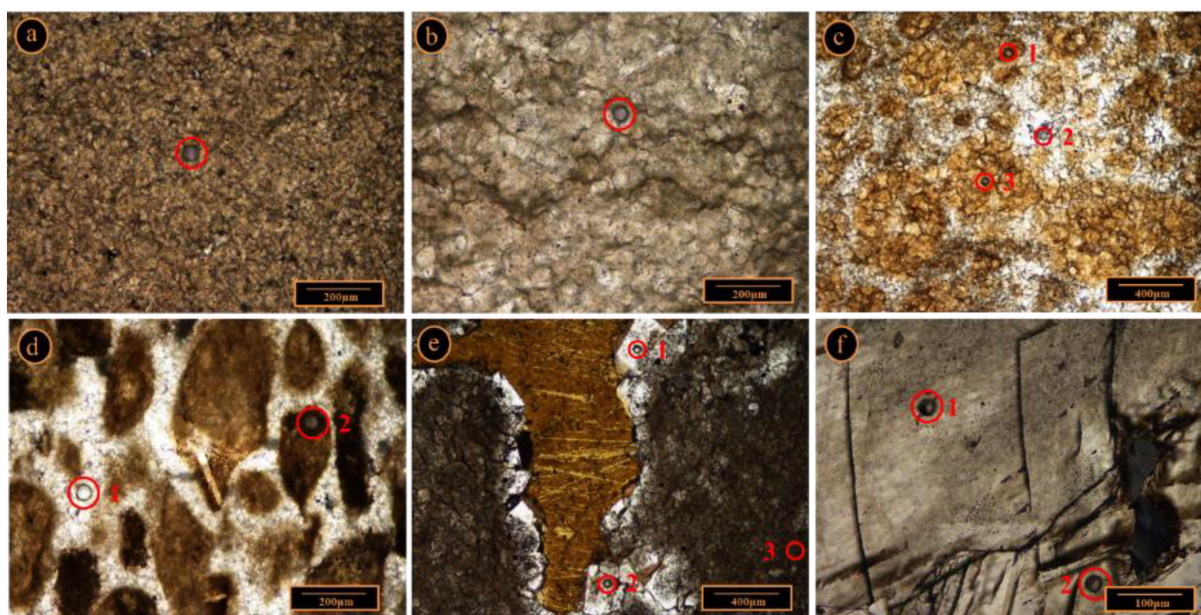


FIGURE 7

Photomicrographs of the spots of LA-ICP-MS analysis. (a) Well YT1-2529.10 m. Dol -1. (b) Well J6-3570.50 m. Dol -2. (c) Well J12-3616.75 m. Dol -3 (spots 1, 3) and dolomite cement (spot 2). (d) Well J6-3585.07 m. Dol -4 (spot 2) and bright dolomite (spot 1). (e) Well J12-3642.41 m. Dol 5 (spots 1, 2) and the surrounding dolomite (spot 3). (f) Well YT1-2529.10 m. Dol -5.

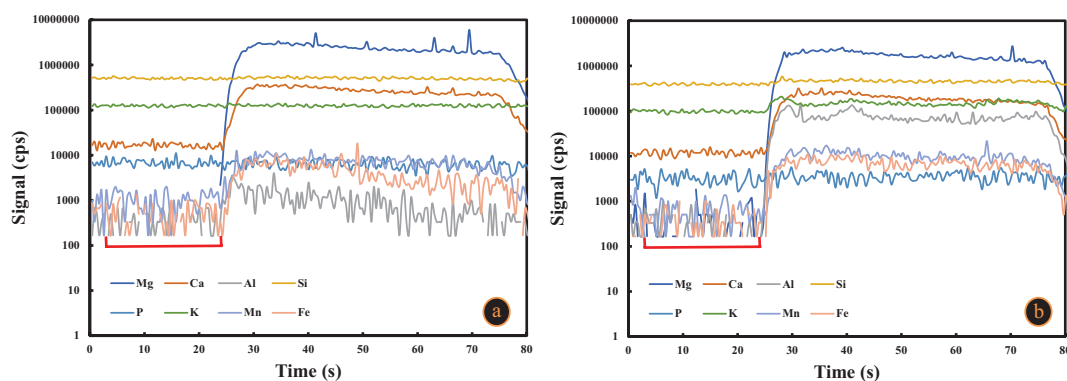


FIGURE 8

(a) Representative single-spot LA-ICP-MS spectra for part elements in the fig.8c spot 3. (b) Representative single-spot LA-ICP-MS spectra for part elements in the fig8f spot 1.

A paleotopographic map of the Ma 5₆ in the study area was drawn using the Ma 5₅ as the standard layer. The map revealed the development of two relatively depressed (I and II) and three relatively uplifted (III, IV, and V) areas (Figure 11). The boundary between the anhydrite and halite deposition areas coincides with the uplift zone. Therefore, the concave paleotopographic structure associated with uplift caused differences in the deposition of evaporites.

The area in the west of the study area where anhydrite was commonly deposited is a supratidal (sabkha) environment. The weak hydrodynamic conditions and restricted water column explains the nodular and elongated morphologies of the anhydrites. However, disturbed mud layers are common on surfaces of cores, and these indicate that the water column was unstable, and this limited the precipitation of evaporites. The common anhydrite-carbonate cycles in the study area illustrate that multiple sub-transgression-regression cycles occurred in the five members of the Majiagou Formation during the major regression. Regarding the east-central parts of the study area where halite was predominantly deposited, depressions were deeper and associated with higher accommodation than in the west. The submarine uplift blocked communication between the depressions and external seawater, thereby restricting them to evaporation environments. At the edge of the east-central area, a thin layer of anhydrite was deposited, while the remaining heavy brine (possibly including heavy brine transported from the west), under the action of water stratification, accumulated from the periphery towards lowlands. This explains the increase in the amount of brine in the low-lying areas, where salinity gradually increased to produce thick halite layers under stable conditions. On surfaces of cores from well F5, halite layers change from dark gray to white, and then to red, from the bottom to the top (Figure 2d). This is because the oldest halite deposits contain mud and carbonate rocks. However, seawater recharge temporarily reduced salinity of the water column, and dissolution of previously deposited halite released some of the mud and carbonate particles, and this accounts for the thin layers of mud or carbonate rocks. The formation of these layers prevented further dissolution of halite, and a drop in the sea level re-ignited seawater

evaporation and downward transportation of brines produced. Halite that was deposited subsequently contains minor muds and carbonates, and this explains its light color. However, salinity of the seawater increased further with increasing evaporation, and the additional halite that was deposited involves K and Mg minerals, and these account for its red color (Eggenkamp et al., 1995). Bao et al. (2004) reported markedly higher K concentrations from the red (0.104–0.220%) relative to the gray and white (0.03–0.06%) halites.

Dolomitization

In addition to petrological and diagenetic characteristics, the origins of different dolomite types were also investigated. The common occurrence of the < 20 μm Dol-1 particles in mud and gypsum suggests that this dolomite type was typically formed during syngenetic to penecontemporaneous periods. Normalized REE patterns for the Dol-1 are similar to those of the micrite (Figure 12a), and these are characterized by weak positive Ce anomalies and almost no Eu anomaly. These results suggest that the Dol-1 is a product of the interaction between evaporating seawater and primary sediments. The bird's-eye formation is evident in sections of its cores, where some gypsum that was incorporated as filling has been dissolved (Figure 3a). Yang et al. (2018) and Xiang et al. (2020) provided evidence from stable isotopes (C, O, Sr) that fluids that produced dolomicrite in the five members of the Majiagou Formation originated from seawater. Results that are presented in the present study suggest that the Dol-1 was formed in a tidal flat that involved intense evaporation.

Conversely, the 50 to 100 μm subhedral to euhedral crystals of the Dol-2, which exhibit comparable sizes in a sample, indicate that this type of dolomite was exposed to weak recrystallization. The similarity of its normalized REE patterns to those of the Dol-1 and micrite indicates that the associated dolomitization fluid originated from seawater (Figure 12b). This dolomite type is usually characterized by brown edges that are attributed to oxidation. The Dol-2 is commonly associated with the Dol-1 in cores. Evidently, this dolomite type was formed via the seepage-reflux

TABLE 3 LA-ICP-MS data of the M5 dolomites in the Ordos Basin.

Types	Spot Number	Na (ppm)	MgCO ₃ (wt%)	Al (ppm)	Si (ppm)	K (ppm)	CaCO ₃ (wt%)	Mn (ppm)	Fe (ppm)	Cu (ppm)	Sr (ppm)	Ba (ppm)
Dol-1	J12-3672.43-1	290.1	42.2	293.1	1143.0	306.2	56.8	15.7	288.4	0.1	131.5	2.5
Dol-1	J12-3648.79-1	117.6	43.2	178.6	1053.5	181.7	56.0	15.0	385.8	0.1	115.8	1.8
Dol-1	J12-3648.79-2	143.6	42.3	299.2	1418.5	407.3	56.6	16.7	407.9	0.3	126.6	3.2
Dol-1	J6-3599.37-1	89.0	42.1	182.4	1073.7	80.3	57.0	16.0	311.4	/	103.0	17.4
Dol-1	J6-3599.37-2	96.8	43.2	290.0	1340.6	96.1	55.8	15.6	312.6	0.1	96.0	1.0
Dol-2	J12-3649.89-1	79.2	42.5	104.8	875.6	55.6	56.8	16.1	347.4	0.5	90.8	1.1
Dol-2	J12-3649.89-2	142.9	39.3	442.6	440.2	345.6	52.3	25.8	1548.9	0.8	102.2	14.8
Dol-2	J12-3646.16-1	351.5	34.4	630.9	2294.2	215.2	45.4	17.4	561.6	0.1	85.2	47.8
Dol-2	J12-3646.16-2	114.8	40.4	262.7	733.2	232.4	53.8	28.3	2201.5	1.8	97.5	7.5
Dol-2	J6-3570.50-1	181.8	41.9	903.3	249.8	197.7	55.7	18.9	566.7	0.4	151.7	4.2
Dol-2	J6-3570.50-2	83.2	42.6	76.8	578.8	120.5	56.9	17.5	323.6	0.0	101.7	0.8
Dol-3	J6-3613.17-1	114.8	37.1	469.4	686.1	639.6	50.0	18.7	398.4	0.4	75.4	4.1
Dol-3	J12-3616.75-1	131.1	40.7	133.3	863.2	82.7	53.8	38.4	1683.7	1.7	74.9	2.9
Dol-3	J12-3616.75-2	181.3	41.4	296.9	618.7	118.9	54.0	32.3	1846.5	3.7	90.3	4.6
Dol-1	J12-3616.75-3	97.6	42.2	360.9	360.8	259.0	57.2	26.0	783.0	0.4	82.9	0.6
Dol-3	J6-3592.14-1	154.1	41.5	91.5	911.6	86.7	57.8	22.1	269.4	0.1	114.6	1.4
Dol-4	J6-3585.07-1	325.6	42.1	868.0	2717.7	1074.9	55.3	34.4	817.5	0.6	110.7	2.4
Cement	J6-3585.07-2	68.8	42.5	33.4	909.5	29.0	56.7	40.3	817.9	/	85.6	0.3
Dol-4	J6-3592.14-1	224.5	41.6	631.9	2172.0	764.1	56.4	23.7	280.1	0.4	119.8	1.5
Dol-4	J6-3613.17-1	79.3	41.4	819.4	2478.4	677.4	56.4	23.2	555.8	/	79.5	6.4
Dol-5-1	YT1-2529.10-1	84.0	40.7	94.0	899.6	22.8	58.7	55.1	142.3	0.1	262.3	0.8
Dol-1	YT1-2529.10-2	106.3	41.8	95.1	326.4	113.5	55.4	29.3	1175.2	0.4	47.0	0.9
Dol-5-1	YT1-2529.10-3	31.7	40.5	179.8	797.4	25.8	58.9	57.2	111.6	/	263.6	0.1
Dol-5-1	J6-3583.10-1	67.3	42.1	50.3	840.5	80.1	57.3	22.2	463.9	0.1	98.2	0.5
Dol-1	J6-3583.10-2	165.2	40.9	431.6	658.4	482.0	54.4	40.3	3877.4	1.9	113.1	20.6
Dol-5-2	J12-3642.41-1	10.3	44.3	4.4	59.6	4.1	55.4	35.6	1007.0	0.2	29.6	0.1
Dol-5-2	J12-3642.41-2	/	42.8	14.3	802.1	0.8	56.6	39.4	1075.8	0.0	50.3	0.0
Dol-1	J12-3642.41-3	169.3	42.1	664.0	2365.3	668.3	56.0	24.9	631.2	0.3	117.6	3.3

TABLE 4 LA-ICP-MS data of the M5 dolomites in the Ordos Basin.

Types	Spot Number	La (ppm)	Ce (ppm)	Pr (ppm)	Nd (ppm)	Sm (ppm)	Eu (ppm)	Gd (ppm)	Tb (ppm)	Dy (ppm)	Ho (ppm)	Er (ppm)	Tm (ppm)	Yb (ppm)	Lu (ppm)	Σ REE	δ Ce	δ Eu
Dol-1	J12-3672.43-1	1.05	1.84	0.22	0.68	0.136	0.028	0.115	0.015	0.103	0.022	0.065	0.008	0.038	0.008	4.33	0.84	0.98
Dol-1	J12-3648.79-1	2.78	6.45	0.61	2.32	0.521	0.089	0.466	0.073	0.374	0.075	0.211	0.028	0.165	0.028	14.19	1.07	0.79
Dol-1	J12-3648.79-2	0.34	1.03	0.11	0.39	0.078	0.013	0.058	0.008	0.060	0.011	0.035	0.006	0.030	0.005	2.17	1.15	0.87
Dol-1	J6-3599.37-1	0.58	1.42	0.12	0.48	0.115	0.023	0.081	0.010	0.073	0.014	0.042	0.006	0.035	0.005	3.00	1.15	1.03
Dol-1	J6-3599.37-2	0.63	1.25	0.16	0.59	0.128	0.025	0.107	0.014	0.095	0.018	0.060	0.011	0.051	0.007	3.14	0.87	0.93
Dol-2	J12-3649.89-1	1.11	2.22	0.23	0.87	0.148	0.026	0.134	0.021	0.118	0.029	0.080	0.011	0.071	0.011	5.07	0.96	0.80
Dol-2	J12-3649.89-2	2.77	6.01	0.58	2.26	0.461	0.078	0.450	0.096	0.486	0.072	0.235	0.037	0.185	0.030	13.74	1.03	0.75
Dol-2	J12-3646.16-1	1.69	5.56	0.63	1.80	0.451	0.061	0.379	0.072	0.387	0.063	0.171	0.023	0.166	0.022	11.47	1.15	0.64
Dol-2	J12-3646.16-2	2.27	3.90	0.34	1.32	0.229	0.047	0.204	0.030	0.172	0.036	0.113	0.017	0.111	0.016	8.80	0.94	0.95
Dol-2	J6-3570.50-1	0.99	1.86	0.18	0.72	0.122	0.020	0.116	0.017	0.093	0.020	0.053	0.007	0.049	0.008	4.27	0.95	0.73
Dol-2	J6-3570.50-2	0.90	1.63	0.16	0.60	0.116	0.020	0.115	0.016	0.084	0.018	0.043	0.007	0.039	0.008	3.76	0.92	0.77
Dol-3	J6-3613.17-1	1.14	2.06	0.21	0.81	0.136	0.026	0.129	0.019	0.112	0.022	0.059	0.008	0.056	0.008	4.79	0.91	0.86
Dol-3	J12-3616.75-1	1.35	3.13	0.35	1.37	0.252	0.048	0.215	0.034	0.195	0.042	0.113	0.016	0.088	0.015	7.21	0.99	0.89
Dol-3	J12-3616.75-2	0.96	2.28	0.25	0.89	0.172	0.031	0.147	0.025	0.138	0.028	0.077	0.010	0.066	0.010	5.09	1.01	0.84
Dol-1	J12-3616.75-3	2.08	6.35	1.02	1.48	0.286	0.063	0.218	0.027	0.057	0.023	0.115	0.003	0.079	0.018	11.82	0.90	1.10
Dol-3	J6-3592.14-1	0.77	1.50	0.16	0.49	0.100	0.021	0.078	0.013	0.068	0.016	0.043	0.006	0.039	0.006	3.30	0.94	1.02
Dol-4	J6-3585.07-1	292.30	1478.60	67.06	1.19	0.112	0.008	1.189	0.029	0.200	0.034	0.229	0.004	0.344	0.010	1841.32	2.30	0.05
Cement	J6-3585.07-2	1.36	5.87	1.05	4.00	1.340	0.124	1.669	0.254	2.067	0.322	0.839	0.117	0.847	0.117	19.98	0.91	0.36
Dol-4	J6-3592.14-1	242.97	1172.79	54.92	1.12	0.116	0.012	0.685	0.039	0.124	0.030	0.042	0.013	0.089	0.005	1472.95	2.21	0.12
Dol-4	J6-3613.17-1	221.26	1120.67	52.85	0.42	0.191	0.038	1.142	0.016	0.050	0.008	0.046	0.004	0.000	0.016	1396.71	2.26	0.24
Dol-5-1	YT1-2529.10-1	0.71	1.57	0.17	0.89	0.203	0.079	0.180	0.028	0.162	0.030	0.108	0.012	0.089	0.013	4.24	0.98	1.80
Dol-1	YT1-2529.10-2	1.11	2.19	0.28	1.23	0.473	0.089	0.329	0.043	0.251	0.047	0.149	0.022	0.129	0.021	6.36	0.86	0.98
Dol-5-1	YT1-2529.10-3	0.77	1.75	0.21	0.95	0.289	0.123	0.238	0.032	0.221	0.029	0.120	0.014	0.127	0.020	4.89	0.95	2.05
Dol-5-1	J6-3583.10-1	1.26	3.64	0.56	1.85	0.371	0.150	0.350	0.069	0.352	0.092	0.230	0.044	0.287	0.030	9.27	0.91	1.81

(Continued)

TABLE 4 Continued

Types	Spot Number	La (ppm)	Ce (ppm)	Pr (ppm)	Nd (ppm)	Sm (ppm)	Eu (ppm)	Gd (ppm)	Tb (ppm)	Dy (ppm)	Ho (ppm)	Er (ppm)	Tm (ppm)	Yb (ppm)	Lu (ppm)	Σ REE	δ Ce	δ Eu
Dol-1	J6-3583.10-2	1.80	5.07	0.70	2.29	0.518	0.099	0.526	0.094	0.392	0.095	0.184	0.033	0.295	0.029	12.12	0.96	0.82
Dol-5-2	J12-3642.41-1	1.36	2.54	0.18	0.53	0.087	0.037	0.103	0.014	0.088	0.011	0.039	0.006	0.026	0.005	5.03	1.07	1.70
Dol-5-2	J12-3642.41-2	1.89	4.55	0.57	1.81	0.328	0.134	0.345	0.058	0.316	0.052	0.108	0.012	0.076	0.012	10.26	0.95	1.73
Dol-1	J12-3642.41-3	1.49	2.95	0.26	0.84	0.228	0.032	0.132	0.024	0.221	0.024	0.057	0.008	0.059	0.005	6.33	1.01	0.78

dolomitization, and some fine dolomites that exhibit effects of dolomitization were probably formed by further dolomitization of the Dol-1 or Dol-3.

Original crystals are visible in the Dol-3, and these generally vary in size from 50 to 100 μ m. Crystals of the associated cement are brighter and finer (10 to 20 μ m) compared to those of the Dol-3. The similarity of its normalized REE patterns to those of the Dol-3 and micrite indicates that the associated dolomitization fluid originated from seawater (Figure 12c). In the sample J12-3616.75, The Σ REEs vary from 3.30 to 5.09 ppm for the Dol-3 (spots 1 and 3) and 11.82 ppm for the cement (spot 2). Dolomites cement has a significantly higher Σ REE than Dol-3. Particles are preferentially dolomitized by Mg-rich fluids because the relatively high porosity and permeability than cements that facilitates seepage dolomitization. The δ Ce values for the Dol-3 range from 0.91 to 1.01, and these values are similar for cement samples (δ Ce=0.90), which indicates that the dolomitization fluid was characterized by sea water. The δ Eu values of dolomite cements have significant positive anomalies than Dol-3. The positive Eu anomalies are attributed to effects of the hydrothermal activities (Hecht et al., 1999) or reducing environment (Khan et al., 2012). Minerals linked to hydrothermal activities are insignificant in the study area, and the concentrations of Mn and Fe for dolomite and cement samples show minor differences. These results suggest that the positive Eu anomaly is not associated with hydrothermal activities. The positive δ Eu anomaly of dolomite in the cement is related to the reducing environment. Eu^{3+} is reduced to Eu^{2+} under reducing conditions, and because the charge and ionic radius of Eu^{2+} are similar to those of Ca^{2+} , Eu^{2+} can replace Ca^{2+} in dolomite, thereby leading to a positive Eu anomaly. These results also indicate that the timing of dolomitization for the Dol-3 and cement differ. The powder samples used to generate geochemical data for fabric-retentive dolomites are worth considering.

Σ REE values for the Dol-4 are high compared to those of other dolomites, and these range from 1396.71 to 1841.32 ppm. There is a great difference normalized REE patterns between the Dol-4 and micrite (Figure 12d). Elevated REEs in this dolomite type are linked to absorption by cell walls of microbes. Compared to the Dol-1 and micrite, the Dol-4 exhibits obvious positive Ce anomalies, and these range from 2.21 to 2.30. In an environment, Ce is sensitive to the redox condition because Ce^{3+} in a fluid is easily oxidized to Ce^{4+} under oxidizing conditions. Compared with Ce^{3+} , Ce^{4+} is insoluble, weakly mobile, and it easily adheres to surfaces of sediments (De Baar et al., 1991; Alibo et al., 1999). These properties explain the negative anomalies of Ce in fluids and positive anomalies in sediments. The lack of prominent Eu anomalies in the Dol-4 indicates that it was deposited in an oxidizing environment. SEM observations revealed the presence of nanoglobule and filiform textures (Figures 5i, j), and these are characteristics of microbial dolomite. Therefore, the high Σ REEs and morphologies of extracellular polymeric substances (EPS) in the Dol-4 suggest that its formation was closely related to microbial activities. Moreover, Liu et al. (2019) reported that planktonic aerobic heterotrophic bacteria in saline lakes can catalyze the formation of primary dolomite, demonstrating that some types of dolomite may represent a biotically induced origin.

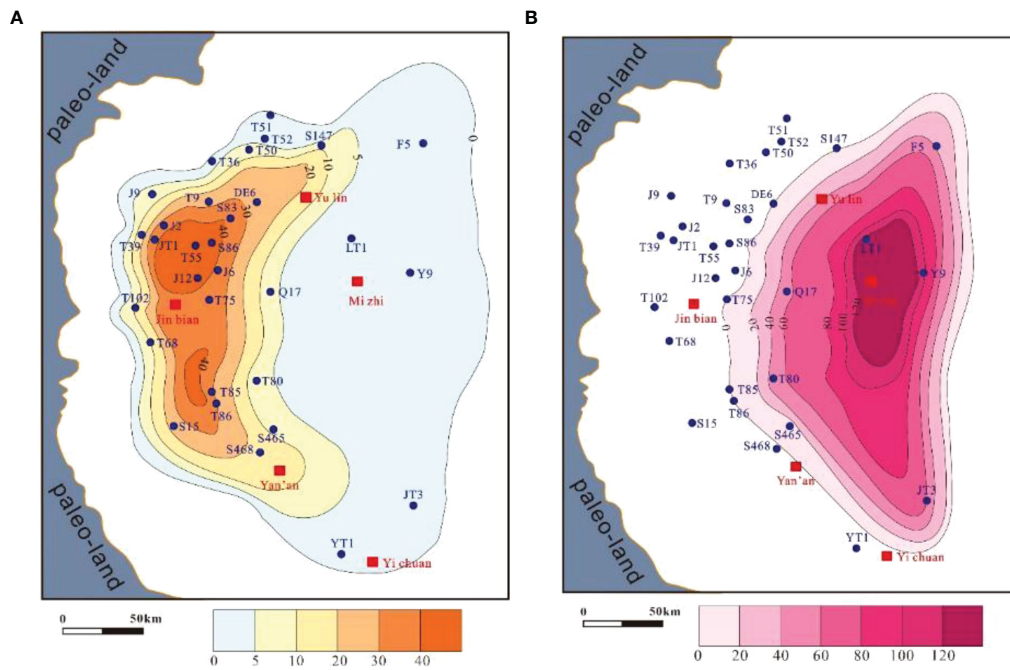


FIGURE 9 (A) Thickness distribution map of anhydrite of M 5 Member in the Ordos Basin. (B) Thickness distribution map of halite of M 5 Member in the Ordos Basin.

The formation of coarse dolomite has been investigated in many studies (Qing and Mountjoy, 1994; Jiang et al., 2016; Noorian et al., 2022). However, conflicting observations have been advanced on the significance of hydrothermal activities in the formation of coarse dolomite. The resemblance of the normalized REE pattern

of the Dol-5-1 to those of the Dol-1 suggests that it is related to surrounding dolomites (Figure 12e). The Dol-5-1 exhibits significant Eu anomalies, and these range from 1.80 to 2.05, with an average value of 1.88. This mean value is markedly higher than the 0.90 that was obtained for surrounding dolomites, and this

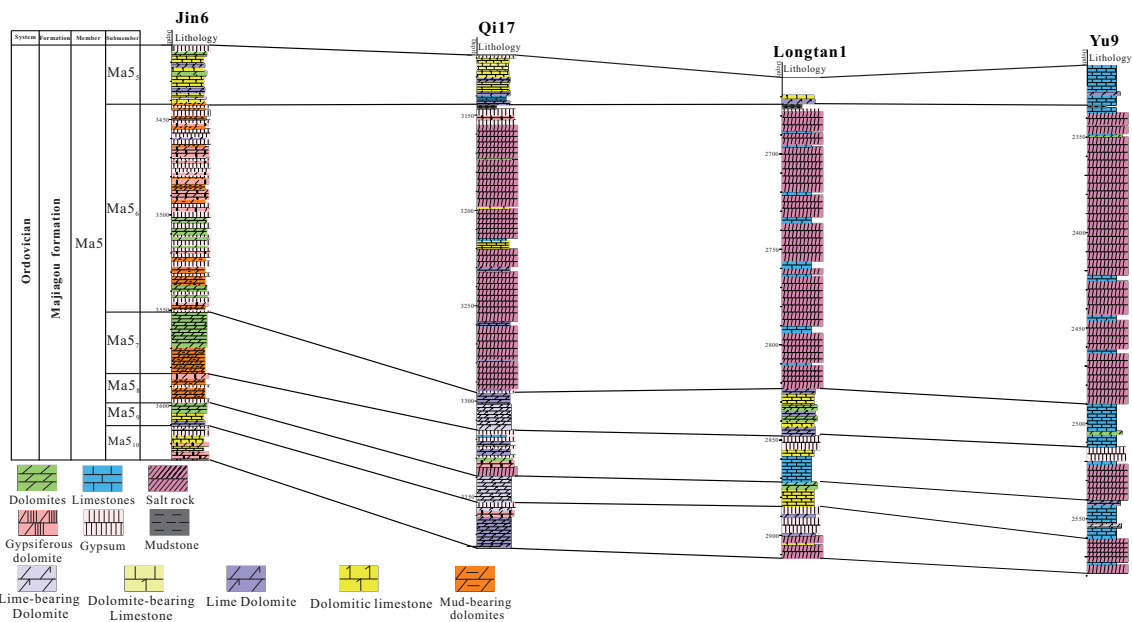
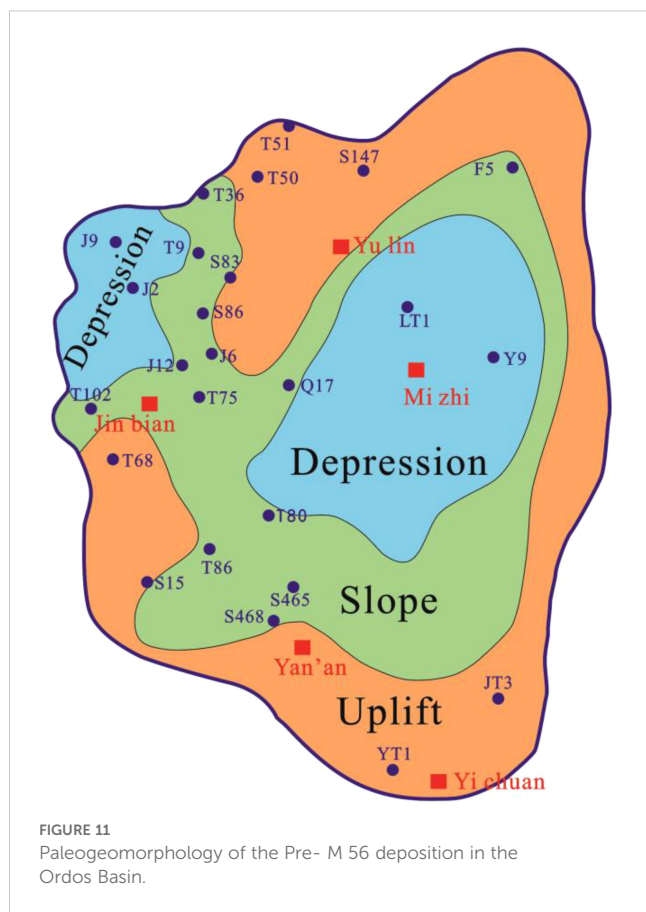


FIGURE 10 The cross section (from J6 to Y9) shows lithologies and thickness of the M 5 Member.



difference suggests that the formation of the Dol-5-1 was probably linked to hydrothermal activities. Zhen et al. (1999) reported homogeneous temperatures of 174.8 to 182.0°C from fluid inclusions in Dol-5-1 in the study area. In the present study, an average homogenization temperature of 130°C was obtained for this type of dolomite. Therefore, according to results that have been presented, the formation of the Dol-5-1 is linked to hydrothermal activities. In the past, the Ordos Basin was considered a stable cratonic basin without large-scale fracture activity in the basement. However, recently, studies have revealed that several fractures are present beneath the sedimentary cover (Wang et al., 2005; Xu et al., 2018), and thus, major fractures probably developed deep in the Ordos Basin.

In the study area, the serrated dolomite cement is another type of coarse dolomite (Dol-5-2). The normalized REE pattern of the Dol-5-2 is similar to those of surrounding dolomites, and these data involve no obvious Ce or Eu anomaly (Figure 12f). Homogeneous temperatures from inclusions in the Dol-5-2 range from 81 to 104°C, and the average is 93.6°C (Figure 7). These results indicate that the formation of the Dol-5-2 was not influenced by hydrothermal fluids, but rather, it probably involved self-regulating dolomitization of early dolomites. During burial, compaction promotes dissolution of dolomite, but in this relatively closed system, re-precipitation occurs. Owing to the close association

between the Dol-5-2 and pores, residual brine in these pores probably contributed to its formation.

Effect of evaporites on dolomitization

The importance of evaporites that are associated with dolomite reservoirs has been highlighted in several studies (Wani and Al-Kabli, 2005; Peyravi et al., 2015). Evaporites are excellent cap rocks because of their low porosity and permeability, as well as resistance to the impacts of diagenesis (Kirkland and Evans, 1981; Jin et al., 2010). In an arid climate, thick evaporites can form, and a restricted environment facilitates seepage-reflux and capillary-concentration dolomitization (Sibley, 1980; Shen et al., 2016). During accumulation in a reservoir, high-maturity hydrocarbons can react with evaporite minerals under high-temperature conditions to generate H₂S via thermochemical sulfate reduction (TSR). This reaction is important for the formation of high-quality reservoirs (Zhu et al., 2006; Jiang et al., 2018). However, the effect of evaporites on the formation of dolomite is another important aspect that remains controversial.

In the present study, the extent of dolomitization in the study area appears related to the type of associated evaporite mineral. Carbonates associated with anhydrite are mostly dolomitized, whereas those linked with halite exhibit partial or no dolomitization (Figure 10). Halite appears to prevent seepage of high Mg²⁺ fluids, and this limits dolomitization when it occurs with carbonates. Conversely, dolomitization seems related to the conversion of gypsum to anhydrite. During burial, the dehydration of gypsum to form anhydrite can absorb Ca²⁺, thereby elevating the Mg²⁺/Ca²⁺ in pore waters in a closed system. The high Mg²⁺ fluids can then migrate via fractures and cause dolomitization of sediments. Therefore, carbonates associated with anhydrite are more susceptible to dolomitization than those linked with halite. This is a new evidence in the study of dolomite problem.

Process of dolomitization

The process of multistage dolomitization in the M5 member in the Ordos Basin can be reconstructed by facies, diagenetic paragenesis and geochemical results, considering the available regional geological and burial history data. The formation process of dolomite in the study can be divided into two phases.

During the initial penecontemporaneous to shallow burial period of the Majiagou Formation, the central paleo uplift created a barrier that restricted water circulation within the study area. Coupled with a dry and hot climate, this led to a progressive increase in seawater salinity. The resulting high-salinity seawater rapidly metasomatized the semi-consolidated sediments, producing Dol-1 and Dol-2 (Figure 13a). Concurrently, sulfate-reducing bacteria in the center of the salinized lake basin facilitated the

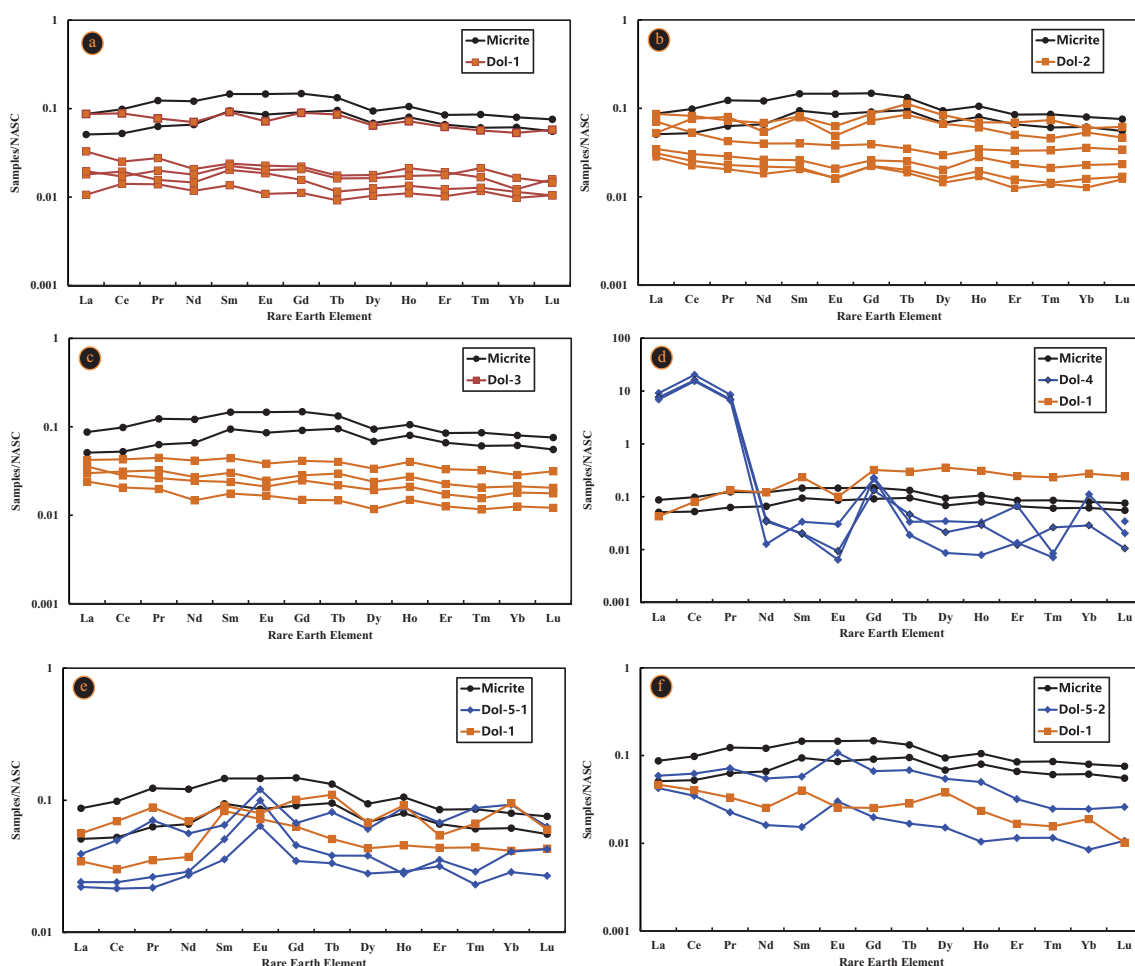


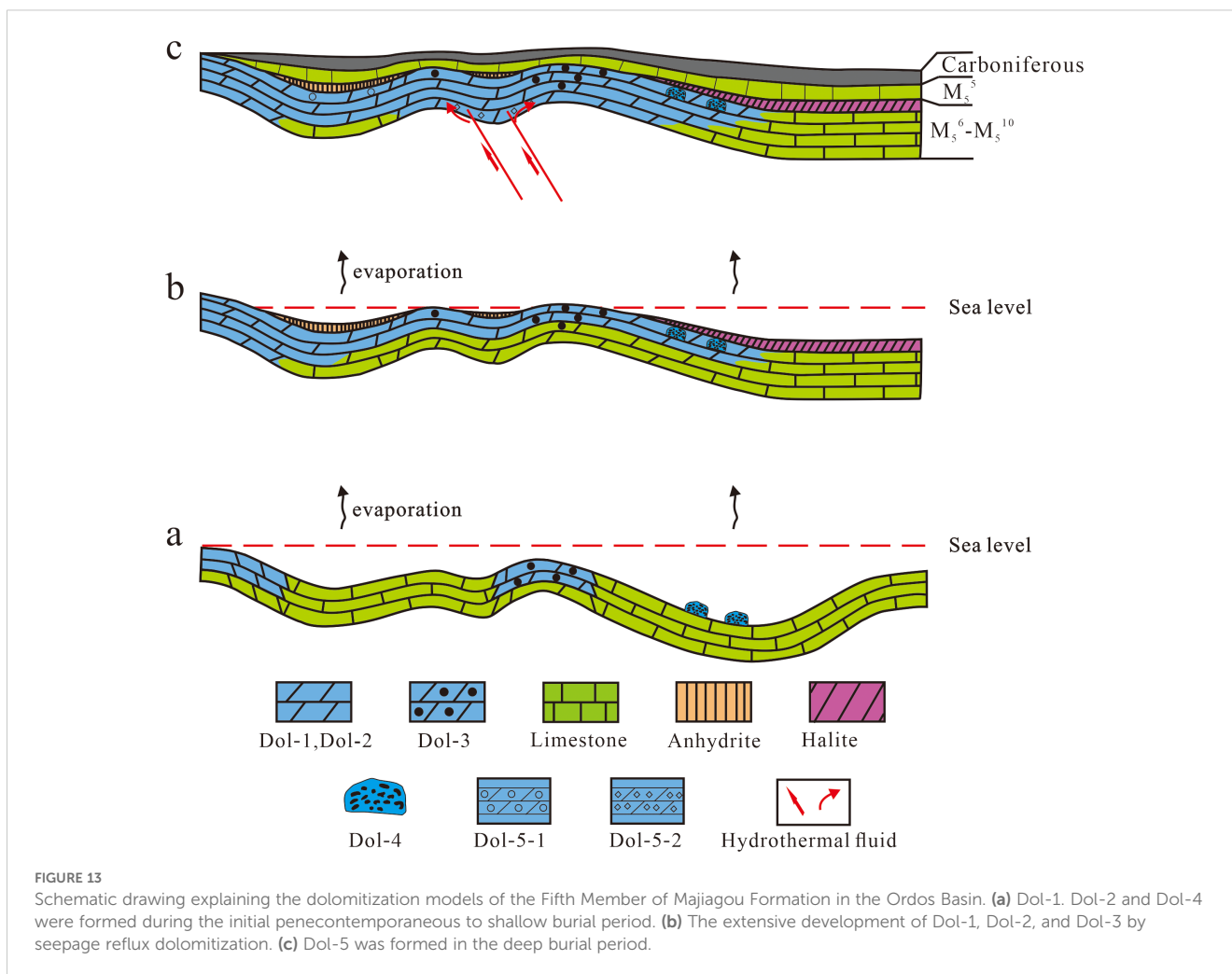
FIGURE 12

North America Shale Composite (NASC; Haskin et al., 1968) normalized REE assemblage patterns of the M5 Member dolomites in the eastern Ordos Basin. (a) Micrite and Dol-1. (b) Micrite and Dol-2. (c) Micrite and Dol-3. (d) Micrite, Dol-4 and Dol-1. (e) Micrite, Dol-5-1 and Dol-1. (f) Micrite, Dol-5-1 and Dol-1.

precipitation of high-magnesium calcite through photosynthesis in a high-salinity brine environment. Over time, the crystal lattice of high-magnesium calcite underwent continuous adjustment, leading to crystal growth and the formation of microbial cell aggregated dolomite. This Dol-4 was subsequently transported to the tidal flat facies zone by tidal forces (Figure 13a). As evaporation continued and gypsum salt rock precipitated, high-salinity seawater rich in Mg^{2+} infiltrated downward through the permeable original sedimentary layers, driven by salinity gradients. Simultaneously, porewater in the sediments reached gypsum saturation and initiated brine reflux driven by water density differences (Rahimpour-Bonab et al., 2010). This seepage reflux dolomitization process persisted for an extended period, spanning from the penecontemporaneous to the shallow burial stages, resulting in extensive dolomite (Dol-1, Dol-2 and Dol-3) distribution throughout the study area (Figure 13b).

The second stage corresponds to the deep burial period. Here, the pressure from overlying strata results in elevated temperatures

and pressures within the pre-salt sequences. Fluids rich in Mg^{2+} , released from overlying Carboniferous clastic rocks abundant in aluminosilicate, could infiltrate pre-salt sequences via strata with high permeability or through concealed fissures and faults, facilitating burial dolomitization (Dol-2, Dol-5). Additionally, the original brine trapped within the eastern gypsum salt rock can migrate along the strata, supplying Mg^{2+} for dolomitization. Geochemical analyses of Dol-5-1 suggest the presence of hydrothermal dolomitization (Figure 13c). While the source of hydrothermal fluids in the Ordos Basin remains contentious, current studies indicate an absence of large-scale basement fault activity necessary for hydrothermal fluid upwelling. Nonetheless, Ren et al. (2007) posited a significant tectonic thermal event during the late Mesozoic, evidenced by notable anomalies in organic matter reflectivity (R_o) near the top surface of the Ordovician. Moreover, although large-scale basement faults have not been conclusively identified in the study area, several hidden basement faults have been detected beneath the sedimentary cover



(Zhao et al., 2003), supporting the potential for hydrothermal dolomite development.

Conclusions

1. Within the study area, five distinct types of dolomite have been identified: micritic (Dol-1), fine-crystalline fabric-obliterative dolomite (Dol-2), fabric-retentive dolomite (Dol-3), microbial mats-associated dolomite (Dol-4), and medium-coarse crystalline dolomite (Dol-5). Geochemical data reveal that the formation of Dol-1, Dol-2, and Dol-3 primarily resulted from seepage-reflux dolomitization and evaporative pumping dolomitization. Dol-4 exhibits clear microbial origins, with associated carbonate particles displaying elongated to elliptical shapes, indicating transport by tidal forces from the gypsum lake basin to the intertidal and supratidal zones after formation. Dol-5-1,
2. In the study area, evaporite types are predominantly gypsum and halite. Sulfur isotope analyses indicate that these evaporites originated from seawater evaporation. The planar distribution of gypsum and halite exhibits certain differences, attributed to paleotopography and varying evaporation intensities. Carbonates underlying gypsum strata exhibit a higher degree of dolomitization compared to those beneath halite strata. This increased dolomitization is due to gypsum absorbing Ca^{2+} and releasing high-salinity brine during its transformation to anhydrite, thereby enhancing the $\text{Mg}^{2+}/\text{Ca}^{2+}$ ratio in the formation fluids.

Data availability statement

The original contributions presented in the study are included in the article/supplementary material. Further inquiries can be directed to the corresponding author.

Author contributions

SF: Conceptualization, Data curation, Formal Analysis, Funding acquisition, Investigation, Methodology, Project administration, Resources, Software, Supervision, Validation, Visualization, Writing – original draft, Writing – review & editing. CZ: Formal Analysis, Funding acquisition, Methodology, Resources, Writing – review & editing. HL: Data curation, Formal Analysis, Writing – original draft. LW: Formal Analysis, Funding acquisition, Investigation, Resources, Supervision, Writing – review & editing. HB: Data curation, Formal Analysis, Funding acquisition, Methodology, Resources, Writing – review & editing. XY: Data curation, Formal Analysis, Writing – original draft. ZS: Writing – review & editing, Supervision. HC: Funding acquisition, Writing – review & editing. LL: Writing – review & editing.

Funding

The author(s) declare that financial support was received for the research and/or publication of this article. This study were funded by the project from the National Natural Science Foundation of China (42202131), Exploration and Development Research Institute of PetroChina Changqing Oilfield Company (2025-230),

References

- Adams, J. E., and Rhodes, M. L. (1960). Dolomitization by seepage refluxion. *AAPG Bull.* 44, 1912–1920. doi: 10.1306/0BDA6263-16BD-11D7-8645000102C1865D
- Alibo, D. S., Nozaki, Y., and Jeandel, C. (1999). Indium and yttrium in North Atlantic and Mediterranean waters: comparison to the Pacific data. *Geochimica cosmochimica Acta* 63, 1991–1999. doi: 10.1016/S0016-7037(99)00080-0
- Bao, H., Yang, C., and Huang, J. (2004). Evaporation drying” and “reinflusing and redissolving” - a new hypothesis concerning formation of the Ordovician evaporites in eastern Ordos Basin. *J. Palaeogeography.* (03), 279–288. doi: 10.3969/j.issn.1671-1505.2004.03.002
- Cai, C., Hu, W., and Worden, R. H. (2001). Thermochemical sulphate reduction in Cambro–Ordovician carbonates in Central Tarim. *Mar. Petroleum Geology.* 18, 729–741. doi: 10.1016/S0264-8172(01)00028-9
- Chang, B., Li, C., Liu, D., Foster, I., Tripati, A., Lloyd, M., et al. (2020). Massive formation of early diagenetic dolomite in the Ediacaran ocean: Constraints on the “dolomite problem. *Proc. Of Natl. Acad. Of Sci. Of United States Of America.* 117, 14005–14014. doi: 10.1073/pnas.1916673117
- Chen, L., Liu, Y., Hu, Z., et al. (2011). Accurate determinations of fifty-four major and trace elements in carbonate by LA-ICP-MS using normalization strategy of bulk components as 100%. *Chem. Geology.* 284, 283–295. doi: 10.1016/j.chemgeo.2011.03.007
- Chen, H., Zhong, Y., Xu, X., Chen, A., Wu, C., Zheng, H., et al. (2014). Types and characteristics of carbonate platform margins of marine carbonate rock in three major basins in western China. *Acta Petrologica Sinica.* 30, 609–621. doi: 10.0000/616a2cb5f0844357a4ba2e73dce75e81
- Claypool, G. E., Holser, W. T., Kaplan, I. R., Sakai, H., and Zak, I. (1980). The age curves of sulfur and oxygen isotopes in marine sulfate and their mutual interpretation. *Chem. geology.* 28, 199–260. doi: 10.1016/0009-2541(80)90047-9
- De Baar, H. J. W., Schijf, J., and Byrne, R. H. (1991). Solution chemistry of the rare earth elements in seawater. *Eur. J. Solid State Inorganic Chem.* 28, 357–73.
- Ding, Z. C., Gao, X., Dong, G. D., Tang, J., Hui, J. T., Wang, S. Y., et al. (2021). Characteristics, genesis and distribution of the Ordovician pre-salt dolomite reservoirs in Ordos Basin. *Mar. Origin Petroleum Geology.* 26, 16–24. doi: 10.3969/j.issn.1672-9854.2021.01.002
- Dong, Y., Chen, H., Wang, J., Hou, M., Xu, S., Zhu, P., et al. (2020). Thermal convection dolomitization induced by the Emeishan Large Igneous Province. *Mar. Petroleum Geology.* 116, 104308. doi: 10.1016/j.marpetgeo.2020.104308
- Eggenkamp, H. G. M., Kreulen, R., and Van Groos, A. F. K. (1995). Chlorine stable isotope fractionation in evaporites. *Geochimica Cosmochimica Acta* 59, 5169–5175. doi: 10.1016/0016-7037(95)00353-3
- Fu, S., Zhang, C., Chen, H., Chen, A., Zhao, J., Su, Z., et al. (2019). Characteristics, formation and evolution of pre-salt dolomite reservoirs in the fifth member of the Ordovician Majiagou Formation, mid-east Ordos Basin, NW China. *Petroleum Explor. Dev.* 46, 1153–1164. doi: 10.1016/S1876-3804(19)60270-3
- Haas, J., Lukoczek, G., Budai, T., and Demeny, A. (2015). Genesis of upper Triassic peritidal dolomites in the Transdanubian Range, Hungary. *Facies* 61, 1–28. doi: 10.1007/s10347-015-0435-7
- Haskin, L. A., Haskin, M. A., Frey, F. A., and Wildeman, T. R. (1968). Relative and absolute terrestrial abundances of the rare earths. *Origin and Distribution of the Elements* (Pergamon), 889–912. doi: 10.1016/B978-0-08-012835-1.50074-X
- Hecht, L., Thuro, K., Plinninger, R., and Cuney, M. (1999). Mineralogical and geochemical characteristics of hydrothermal alteration and episyenitization in the Königshain granites, northern Bohemian Massif, Germany. *Int. J. Earth Sci.* 88, 236–252. doi: 10.1007/s005310050262

Key science and technology projects of PetroChina Changqing Oilfield Company (CQZDZX2024). PetroChina Changqing Oilfield Company was not involved in the study design, collection, analysis, interpretation of data, the writing of this article, or the decision to submit it for publication.

Conflict of interest

Authors LW and HB were employed by PetroChina Changqing Oilfield Company.

The remaining authors declare that the research was conducted in the absence of any commercial or financial relationships that could be construed as a potential conflict of interest.

Generative AI statement

The author(s) declare that no Generative AI was used in the creation of this manuscript.

Publisher’s note

All claims expressed in this article are solely those of the authors and do not necessarily represent those of their affiliated organizations, or those of the publisher, the editors and the reviewers. Any product that may be evaluated in this article, or claim that may be made by its manufacturer, is not guaranteed or endorsed by the publisher.

- Hovorka, S. D. (1992). Halite pseudomorphs after gypsum in bedded anhydrite; clue to gypsum-anhydrite relationships. *J. Sedimentary Research*. 62, 1098–1111. doi: 10.1306/D4267A5F-2B26-11D7-8648000102C1865D
- Hsü, K. J., and Siegenthaler, C. (1969). Preliminary experiments on hydrodynamic movement induced by evaporation and their bearing on the dolomite problem. *Sedimentology* 12, 11–25. doi: 10.1111/j.1365-3091.1969.tb00161.x
- Hsü, K. J., Stoffers, P., and Ross, D. A. (1978). Messinian evaporites from the Mediterranean and Red Seas. *Mar. Geology*. 26, 71–72. doi: 10.1016/0025-3227(78)90046-4
- Iannace, A., Capuano, M., and Galluccio, L. (2011). Dolomites and dolomites in Mesozoic platform carbonates of the Southern Apennines: Geometric distribution, petrography and geochemistry. *Palaeogeography Palaeoclimatology Palaeoecology*. 310, 324–339. doi: 10.1016/j.palaeo.2011.07.025
- Jafarian, A., Fallah, R., Mattern, F., and Heubeck, C. (2017). Reservoir quality along a homoclinal carbonate ramp deposit: The Permian Upper Dalan Formation, South Pars Field, Persian Gulf Basin. *Mar. Petroleum Geology*. 88, 587–604. doi: 10.1016/j.marpetgeo.2017.09.002
- Ji, Y., Zhang, S., and Feng, J. (2005). Relationship between paleotopography and volumetric change rate of lacustrine basin to the sequence structure. *Acta Sedimentologica Sin.* 23, 631. doi: 10.3969/j.issn.1000-0550.2005.04.011
- Jiang, L., Cai, C. F., Worden, R. H., Crowley, S. F., Jia, L., Zhang, K., et al. (2016). Multiphase dolomitization of deeply buried Cambrian petroleum reservoirs, Tarim Basin, north-west China. *Sedimentology* 63, 2130–2157. doi: 10.1111/sed.2016.63.issue-7
- Jiang, L., Worden, R. H., Cai, C. F., Li, K., Xiang, L., Cai, L., et al. (2014). Dolomitization of gas reservoirs: the upper Permian Changxing and lower Triassic feixianguan formations, northeast Sichuan Basin, China. *J. Sedimentary Res.* 84, 792–815. doi: 10.2110/j.sr.2014.65
- Jiang, L., Worden, R. H., Cai, C. F., Shen, A., and Crowley, S. F. (2018). Diagenesis of an evaporite-related carbonate reservoir in deeply buried Cambrian strata, Tarim Basin, northwest China. *AAPG Bulletin*. 102, 77–102. doi: 10.1306/0328171608517048
- Jin, Z., Zhou, Y., Yun, J., Sun, D., and Long, S. (2010). Distribution of gypsum-salt cap rocks and near-term hydrocarbon exploration targets in the marine sequences of China. *Oil Gas Geology*. 31, 715–724. (in Chinese with English abstract). doi: CNKI: SUN:SYTT.0.2010-06-007
- Kakemem, U., Jafarian, A., Husinec, A., Adabi, M. H., and Mahmoudi, A. (2021). Facies, sequence framework, and reservoir quality along a Triassic carbonate ramp: Kangan Formation, South Pars Field, Persian Gulf Superbasin. *J. Petroleum Sci. Engineering*. 198, 108166. doi: 10.1016/j.petrol.2020.108166
- Kaufman, J. (1994). Numerical models of fluid flow in carbonate platforms: implications for dolomitization. *J. Sedimentary Res.* 64, 128–139. doi: 10.1306/D4267D2F-2B26-11D7-8648000102C1865D
- Khan, K. F., Dar, S. A., and Khan, S. A. (2012). Rare earth element (REE) geochemistry of phosphorites of the Sonrai area of Paleoproterozoic Bijawar basin, Uttar Pradesh, India. *J. Rare Earths*. 30, 507–514. doi: 10.1016/S1002-0721(12)60081-7
- Kim, J., Kimura, Y., Puchala, B., Yamazaki, T., Becker, U., Sun, W., et al. (2023). Dissolution enables dolomite crystal growth near ambient conditions. *Science* 384, 915–920. doi: 10.1126/science.adi3690
- Kirkland, D. W., and Evans, R. (1981). Source-rock potential of evaporitic environment. *AAPG Bulletin*. 65, 181–190. doi: 10.1306/2F918EF5-16CE-11D7-8645000102C1865D
- Li, J., Zhang, W., Luo, X., and Hu, G. (2008). Paleokarst reservoirs and gas accumulation in the *gbian field, Ordos Basin. *Mar. Petroleum Geology*. 25, 401–415. doi: 10.1016/j.marpetgeo.2008.01.005
- Lith, Y. V., Warthmann, R., Vasconcelos, C., and Mckenzie, J. A. (2010). Microbial fossilization in carbonate sediments: a result of the bacterial surface involvement in dolomite precipitation. *Sedimentology* 50, 237–245. doi: 10.1046/j.1365-3091.2003.00550.x
- Liu, Y., Gao, S., Kelemen, P. B., and Xu, W. (2008a). Recycled crust controls contrasting source compositions of Mesozoic and Cenozoic basalts in the North China Craton. *Geochimica cosmochimica Acta* 72, 2349–2376. doi: 10.1016/j.gca.2008.02.018
- Liu, Y., Hu, Z., Gao, S., Guenther, D., Xu, J., Gao, C., et al. (2008b). *In situ* analysis of major and trace elements of anhydrous minerals by LA-ICP-MS without applying an internal standard. *Chem. Geology*. 257, 34–43. doi: 10.1016/j.chemgeo.2008.08.004
- Liu, D., Yu, N., Papineau, D., Fan, Q., Wang, H., Qiu, X., et al. (2019). The catalytic role of planktonic aerobic heterotrophic bacteria in protodolomite formation: Results from Lake Jibuhulangu Nuur, Inner Mongolia, China. *Geochimica Et Cosmochimica Acta* 263, 31–49. doi: 10.1016/j.gca.2019.07.056
- Lonnee, J., and Machel, H. G. (2006). Pervasive dolomitization with subsequent hydrothermal alteration in the Clarke Lake gas field, Middle Devonian Slave Point Formation, British Columbia, Canada. *AAPG bulletin*. 90, 1739–1761. doi: 10.1306/03060605069
- Lu, F. H., and Meyers, W. J. (1998). Massive dolomitization of a late Miocene carbonate platform: a case of mixed evaporative brines with meteoric water, Nijar, Spain. *Sedimentology* 45, 263–277. doi: 10.1046/j.1365-3091.1998.0142e.x
- Machel, H. G., and Lonnee, J. (2002). Hydrothermal dolomite—A product of poor definition and imagination. *Sedimentary geology*. 152, 163–171. doi: 10.1016/S0037-0738(02)00259-2
- Manaa, A. A., and Aref, M. A. (2022). Microbial mats and evaporite facies variation in a supralittoral, ephemeral lake, Red Sea coast, Saudi Arabia. *Facies* 68, 1–21. doi: 10.1007/s10347-021-00641-0
- Manzi, V., Gennari, R., Lugli, S., Roveri, M., Scafetta, N., Schreiber, B. C., et al. (2012). High-frequency cyclicity in the Mediterranean Messinian evaporites: evidence for solar-lunar climate forcing. *J. Sedimentary Res.* 82, 991–1005. doi: 10.2110/j.sr.2012.81
- Middleton, K., Coniglio, M., Sherlock, R., and Frappe, S. K. (1993). Dolomitization of Middle Ordovician carbonate reservoirs, southwestern Ontario. *Bull. Can. Petroleum Geology*. 41, 150–163. doi: 10.35767/gscpubbull.41.2.150
- Mitchell, N. C., Shi, W., Izzeldin, A. Y., and Stewart, I. (2021). Reconstructing the level of the central Red Sea evaporites at the end of the Miocene. *Basin Res.* 33, 1266–1292. doi: 10.1111/bre.12513
- Natalicchio, M., Pellegrino, L., Clari, P., Pastoro, L., and Dela, P. F. (2021). Gypsum lithofacies and stratigraphic architecture of a Messinian marginal basin (Piedmont Basin, NW Italy). *Sedimentary Geology*. 425, 106009. doi: 10.1016/j.sedgeo.2021.106009
- Noorian, Y., Moussavi-Harami, R., Hollis, C., Reijmer, J., Mahboubi, A., Omidpour, A., et al. (2022). Control of climate, sea-level fluctuations and tectonics on the pervasive dolomitization and porosity evolution of the Oligo-Miocene Asmari Formation (Dezful Embayment, SW Iran). *Sedimentary Geology*. 427, 106048. doi: 10.1016/j.sedgeo.2021.106048
- Peyravi, M., Rahimpour-Bonab, H., Nader, F. H., and Kamali, M. R. (2015). Dolomitization and burial history of lower triassic carbonate reservoir-rocks in the Persian Gulf (Salman offshore field). *Carbonates Evaporites* 30, 25–43. doi: 10.1007/s13146-014-0197-2
- Qing, H., and Mountjoy, E. W. (1994). Rare earth element geochemistry of dolomites in the Middle Devonian Presqu'île barrier, Western Canada Sedimentary Basin: implications for fluid-rock ratios during dolomitization. *Sedimentology* 41, 787–804. doi: 10.1111/j.1365-3091.1994.tb01424.x
- Rahimpour-Bonab, H., Esrafil-Dizaji, B., and Tavakoli, V. (2010). Dolomitization and anhydrite precipitation in permo-triassic carbonates at the South Pars gasfield, offshore Iran: controls on reservoir quality. *J. Petroleum Geology*. 33, 43–66. doi: 10.1111/j.1747-5457.2010.00463.x
- Ren, Z., Cui, J., Li, J., Wang, J., Guo, K., Wang, W., et al. (2014). Tectonic-thermal history reconstruction of Ordovician in the Weibei uplift of Ordos Basin. *Acta Geologica Sinica*. 88, 2044–2056. doi: 10.3969/j.issn.0001-5717.2014.11.003
- Ren, Z., Zhang, S., Gao, S., Cui, J., Xiao, Y., Xiao, H., et al. (2007). Tectonic thermal history and its significance on the formation of oil and gas accumulation and mineral deposit in Ordos Basin. *Sci. China Ser. D: Earth Sci.* 50, 27–38. doi: 10.1007/s11430-007-6022-1
- Riding, R. (2000). Microbial carbonates: the geological record of calcified bacterial-algal mats and biofilms. *Sedimentology* 47, 179–214. doi: 10.1046/j.1365-3091.2000.00003.x
- Ryan, B. H., Kaczmarek, S. E., and Rivers, J. M. (2020). Early and pervasive dolomitization by near-normal marine fluids: New lessons from an Eocene evaporative setting in Qatar. *Sedimentology* 67, 2917–2944. doi: 10.1111/sed.12726
- Schreiber, B. C., and Tabakh, M. E. (2000). Deposition and early alteration of evaporites. *Sedimentology* 47, 215–238. doi: 10.1046/j.1365-3091.2000.00002.x
- Shen, A., Zheng, J., Chen, Y., Ni, X., and Huang, L. (2016). Characteristics, origin and distribution of dolomite reservoirs in Lower-Middle Cambrian, Tarim Basin, NW China. *Petroleum Explor. Dev.* 43, 340–349. doi: 10.1016/S1876-3804(16)30044-1
- Sibley, D. F. (1980). Climatic control of dolomitization, Seroc Domi Formation (Pliocene), Bonaire, NA. *Special Publications*. doi: 10.2110/pec.80.28.0247
- Su, Z., Zhang, L., Li, Q., and Chi, G. (2017). Characteristics of fluid inclusions in dolomite of the Ordovician majiagou formation in the Ordos basin and their significance. *Bull. Mineralogy, Petrology Geochemistry*. 36, 843–849. doi: CNKI: SUN: KYDH.0.2017-05-018
- Sun, D., Li, B., Ma, Y., and Liu, Q. (1995). An investigation on evaporating experiments for Qinghai lake water, China. *J. Salt Lake Science*. 02, 10–19. Available online at: <http://ir.isl.ac.cn/handle/363002/124>.
- Treesh, M. I., and Friedman, G. M. (1974). “Sabkha deposition of the Salina group (Upper Silurian) of New York state,” in *Fourth Symposium on salt*, vol. 1. (Northern Ohio Geological Society, Cleveland), 34–46.
- Vasconcelos, C., McKenzie, J. A., Bernasconi, S., Grujic, D., and Tien, A. (1995). Microbial mediation as a possible mechanism for natural dolomite formation at low temperatures. *Nature* 377, 220–222. doi: 10.1038/377220a0
- Wang, Z., Zhao, W., Men, X., Zhen, H., and Li, X. (2005). Control of basement fault minor-activity on gas pool formation of Upper Paleozoic, Ordos Basin. *Shiyou Kantan Yu Kaifa(Petrol. Explor. Dev.)*. 32, 9–13. doi: 10.1016/j.molcatb.2005.02.001
- Wani, M. R., and Al-Kabli, S. K. (2005). *Sequence Stratigraphy and Reservoir Characterization of The 2nd. Eocene Dolomite Reservoir, Wafra Field, Divided Zone, Kuwait-Saudi Arabia*[C]. doi: 10.2118/92827-MS
- Warren, J. (2000). Dolomite: occurrence, evolution and economically important associations. *Earth Sci. Rev.* 52, 1–81. doi: 10.1016/S0012-8252(00)00022-2

- Warren, J. K. (2006). *Evaporites: Sediments, Resources and Hydrocarbons [M]*. (Berlin, Heidelberg: Springer)
- Wotte, T., Shields-Zhou, G. A., and Strauss, H. (2012). Carbonate-associated sulfate: Experimental comparisons of common extraction methods and recommendations toward a standard analytical protocol. *Chem. Geology*. 326, 132–144. doi: 10.1016/j.chemgeo.2012.07.020
- Xiang, P., Ji, H., Shi, Y., Huang, Y., Sun, Y., Xu, X., et al. (2020). Petrographic, rare earth elements and isotope constraints on the dolomite origin of Ordovician Majiagou Formation (Jizhong Depression, North China). *Mar. Petroleum Geology*. 117, 104374. doi: 10.1016/j.marpetgeo.2020.104374
- Xiao, D., Cao, J., Tan, X., Xiong, Y., Zhang, D., Dong, G., et al. (2021). Marine carbonate reservoirs formed in evaporite sequences in sedimentary basins: A review and new model of epeiric basin-scale moldic reservoirs. *Earth-Science Rev.* 223, 103860. doi: 10.1016/j.earscirev.2021.103860
- Xiong, Y., Tan, X., Zuo, Z., Wang, J., Ni, C., Shen, A., et al. (2019). Middle Ordovician multi-stage penecontemporaneous karstification in North China: Implications for reservoir genesis and sea level fluctuations. *J. Asian Earth Sci.* 183, 103969. doi: 10.1016/j.jseas.2019.103969
- Xiong, L., Yao, G., Xiong, S., Wang, J., Ni, C., Shen, A., et al. (2018). Origin of dolomite in the Middle Devonian Guanwushan Formation of the western Sichuan Basin, western China. *Palaeogeography Palaeoclimatology Palaeoecology*. 495, 113–126. doi: 10.1016/j.palaeo.2017.12.035
- Xu, Q., Shi, W., Xie, X., Bushey, A., Xu, L., Wu, R., et al. (2018). Inversion and propagation of the Late Paleozoic Porjianghaizi fault (North Ordos Basin, China): Controls on sedimentation and gas accumulations. *Mar. Petroleum Geology*. 91, 706–722. doi: 10.1016/j.marpetgeo.2018.02.003
- Yang, H., and Bao, H. (2011). Characteristics of hydrocarbon accumulation in the middle Ordovician assemblages and their significance for gas exploration in the Ordos Basin. *Natural Gas Industry* 31, 11–20 + 124. doi: 10.3787/j.issn.1000-0976.2011.12.003
- Yang, H., Fu, J., Wei, X., and Liu, X. (2008). Sulige field in the Ordos Basin: Geological setting, field discovery and tight gas reservoirs. *Mar. Petroleum Geology*. 25, 387–400. doi: 10.1016/j.marpetgeo.2008.01.007
- Yang, X., Mei, Q., Wang, X., Dong, Z., Li, Y., Huo, F., et al. (2018). Indication of rare earth element characteristics to dolomite petrogenesis—A case study of the fifth member of Ordovician Majiagou Formation in the Ordos Basin, central China. *Mar. Petroleum Geology*. 92, 1028–1040. doi: 10.1016/j.marpetgeo.2017.12.004
- Zhang, Z., Yang, X., and Dong, Z. (2016). Characteristics and genesis of Ordovician Majiagou Submember-5–5 dolostone in middle assemblage, Ordos Basin. *Mar. Origin Petroleum Geology*. 21, 65–71. doi: 10.3969/j.issn.1672-9854.2016.02.008
- Zhao, J., Chen, H., and Xiang, F. (2003). The high-resolution sequence stratigraphy feature of Yanan Formation in Yanan area, Ordos basin. *Acta Sedimentologica Sinica*. 21, 307. doi: 10.3969/j.issn.1000-0550.2003.02.018
- Zhao, W., Zhang, Y., Zhao, C., and Xu, D. (1996). Formation and distribution of coal measure – derived hydrocarbon accumulation in NW China. *Acta Petrolei Sinica*. 02), 1–8.
- Zhao, W. W., and Zhou, M. F. (2015). *In-situ* LA-ICP-MS trace elemental analyses of magnetite: The Mesozoic Tengtie skarn Fe deposit in the Nanling Range, South China. *Ore Geology Rev.* 65, 872–883. doi: 10.1016/j.oregeorev.2014.09.019
- Zhen, B. Y., Ye, J., Zhu, Z. Q., and Song, G. C. (1999). Study of the fluid inclusions from the Majiagou Formation of Ordovician, Ordos Basin. *J. Xi'an Eng. University*. 21, 13–16. (in Chinese with English abstract). doi: 10.3969/j.issn.1672-6561.1999.03.004
- Zhou, J. G., Zhang, F., Guo, Q. X., Deng, H. Y., and Xin, Y. G. (2011). Barrier-lagoon sedimentary model and reservoir distribution regularity of Lower-Ordovician Majiagou Formation in Ordos Basin. *Acta Sedimentol Sin.* 29, 64–71. (in Chinese with English abstract). doi: 10.14027/j.cnki.cjxb.2011.01.013
- Zhu, J., Chen, L., Ji, Y., and Li, G. (2006). Influence factors for development of the Upper Paleozoic pore in thrust belt of western Ordos Basin. *Acta Petrolei Sinica*. 27, 37. doi: 10.3321/j.issn:0253-2697.2006.03.008
- Zhu, D., Meng, Q., Jin, Z., Liu, Q., and Hu, W. (2015). Formation mechanism of deep Cambrian dolomite reservoirs in the Tarim basin, northwestern China. *Mar. Petroleum Geology*. 59, 232–244. doi: 10.1016/j.marpetgeo.2014.08.022